Properties of bound, resonant, and regular continuum states of the excitation spectrum of symmetric liquid ^{4}He films at $T=0$ K

Leszek Szybisz*
Laboratorio Tandem Argentino, Departamento de Física, Comisión Nacional de Energía Atómica, Av. del Libertador 8250, RA-1429 Buenos Aires, Argentina
and Departamento de Física, Facultad de Ciencias Exactas y Naturales, Universidad de Buenos Aires, Ciudad Universitaria, RA-1428 Buenos Aires, Argentina
(Received 6 July 1995)

Elementary excitations in rather thick symmetric films of liquid ^{4}He at $T=0$ K are investigated. They are characterized by a momentum $\hbar\mathbf{q}$ parallel to the surface and may be described by bound or continuum states, which are obtained by solving a Bogoliubov-type equation formulated within the framework of the paired-phonon analysis and the hypernetted-chain approximation. Films of coverages $n_c=0.3$ and 0.4 Å^{-2} confined by simple Gaussian potentials are studied. The excitation spectrum is numerically evaluated by discretizing the associated eigenvalue problem in a finite box. The evolution of the energy levels as a function of the box size is explored. Examples of the calculated energies and wave functions are displayed in a series of figures. Two differing sorts of continuum states may be distinguished. Depending on the behavior of their excitation energies as a function of the box size on the one hand, and the spatial distribution of their wave functions inside the film and in the asymptotic region far apart from the interface layer on the other, the continuum solutions can be separated into two classes of excitations: (a) the ''regular'' continuum states and (b) the ''resonant modes.'' The matrix elements of the particle-hole potential and the penetration factors of the most important states are examined. The lowest-lying branch of states is always bound and for $q<q_R$ ($q_R\simeq 1.9$ Å^{-1} being the momentum at the roton minimum) it describes surface ripplon excitations. In the atomic scale regime, 1.1 Å$^{-1}<q<q_R$, the hardest ''resonant mode'' can be interpreted as a roton trapped at the center of the film and therefore associated with ''bulk'' excitations of the system. Our results support the occurrence of the repulsion between ''bulk'' and ripplon excitations proposed by Pitaevskii and Stringari. The strength of contributions originated from different normal modes to the liquid structure function is evaluated. While for very small values of momenta ($q\leqslant 0.2$ Å^{-1}) the contribution of the lowest-lying normal mode is dominant, for momenta $q>q_R$ the structure factor is determined by the contributions originated from the three lowest-lying even states. At $q\approx q_R$ there is a dramatic transfer of strength from the bound continuation of the hardest ''resonant mode'' to the ripplon excitation. Experimental data of the inelastic structure factor $S(q,\hbar\omega)$ may be satisfactorily interpreted on the basis of our calculation. On the other hand, it is shown that for $2.9\leqslant q\leqslant 3.9$ Å^{-1} the lowest-lying excitations become surface modes again.

I. INTRODUCTION

In a recently published review article Cheng *et al.*[1] emphasize the increasing interest in studies of properties of liquid ^{4}He interfaces and surfaces. As a matter of fact, there is a continuous development in the experiment and the theory of such systems. A variety of theoretical pictures have been adopted in order to interpret experimental results.[1] In particular, much work has been devoted in recent years in order to apply a variational procedure based on the theory of correlated basis functions[2–4] (CBF's) for understanding the behavior of inhomogeneous liquid ^{4}He at zero absolute temperature[5–22] as well as at finite temperatures.[23–25]

Perhaps one of the most interesting issues in this field is the investigation of elementary excitations[26] of surfaces of liquid ^{4}He. Among other problems currently studied, it is worthwhile to mention the observation of an oscillatory dependence of the third-sound velocity c_3 on film thickness for thin films.[14–16,27] In the present work we shall concentrate on a microscopic analysis of the properties of elementary excitations in liquid ^{4}He films at $T=0$. There is a great theoretical as well as experimental activity in this area. Excitations in ^{4}He films have been measured in the atomic wavelength regime by using neutron scattering techniques.[28,29] This measurement has motivated a renewal of theoretical efforts devoted to understanding the nature of excitations.

The excitation spectrum of a semi-infinite ^{4}He fluid at vanishing temperature has been explored by Chang and Cohen[30] (see also the review by Edwards and Saam[31]) within the framework of the variational many-body theory. Such a system presents a density profile at $z\simeq 0$, and the density approaches 0 as $z\rightarrow+\infty$ and reaches the bulk density ρ_∞ as $z\rightarrow-\infty$. In the case of a planar symmetry excitations depend on the momentum $\hbar\mathbf{q}$ parallel to the surface. More recently, employing the CBF theory Gernoth *et al.*[22–25] have investigated excitations in a planar ^{4}He interface at various temperatures, $0\leqslant T\leqslant 2$ K, under vapor-liquid saturation conditions. As an example of the application of a different approach in order to describe the inhomogeneous free ^{4}He surface at temperature $T=0$ we can mention the paper of Ji and Wortis.[32] These authors have used a semiphenomenological Landau model to interpret surface phenomena and

put a special emphasis in the analysis of continuum states of the excitation spectrum. On the other hand, the CBF method has been applied to get information about excitations of symmetric finite films at vanishing temperature in.[6,7,17–21] These systems present a central density ρ_c and two symmetric profiles where the density approaches 0 as $z \to \pm\infty$ (cf. Fig. 5 in Ref. 17). Furthermore, excitations of realistic systems such as finite films adsorbed to solid substrates have been also analyzed within CBF theory by Krotscheck and co-workers.[8,10,12,13,15,16]

It is known that the lowest-lying excitations of a strongly correlated quantum many-body system in the long-wavelength limit (i.e., at small values of momentum q) are surface ripplons which may be described within the framework of simple hydrodynamic models.[31,33,34] It has been shown[9,21,22] that results obtained for physical observables within the CBF method for small momenta agree with the hydrodynamic predictions. However, Atkins'[33] description is not adequate for momenta corresponding to atomic wavelengths ($q \sim 1$ Å^{-1}) because the behavior of ripplons at these momenta is not governed by laws resembling classical hydrodynamics. In a more recent paper, Pitaevskii and Stringari[35] have used the Green's function formalism within a quantized hydrodynamic description in order to estimate the lowest-lying (ripplon) dispersion curve close to the roton minimum ($q_R \simeq 1.9$ Å^{-1}). They found that due to the interaction between surface ripplons and bulk roton excitations (which has been suggested many years before by Edwards *et al.*[31,34]) the ripplon dispersion relation remains below the energy of bulk rotons.

Let us now focus our attention on the most recent theoretical advances within CBF theory concerning the excitations in nonuniform ^{4}He at $T=0$. As mentioned before, several properties have been explored: (i) by studying a semi-infinite system[22,24] and (ii) by investigating layered films adsorbed on substrates.[13,15,16] Gernoth and Ristig performed a classification of continuum states taking into account the behavior of wave functions and excitation energies $\hbar\omega_\kappa(q)$; the quantum number κ labels the eigenstates. The latter results were mapped onto a $\hbar\omega$ vs q plot and compared with the known results for a bulk system (see Fig. 9 in Ref. 24). Furthermore, in a subsequent paper[22] the ripplon dispersion relation and the associated wave functions were analyzed for $0 \leqslant q \leqslant q_R$. From the behavior at small momenta the third-sound velocity c_3 was evaluated. At atomic wavelengths (1 Å$^{-1} \leqslant q \leqslant q_R$) the wave functions associated with ripplons are localized in the surface layer, their energies approaching the bulk roton energy at the characteristic wavelength $q \simeq q_R$. These states were interpreted as trapped rotons. On the other hand, Krotscheck and Tymczak[13] discussed layered films for three coverages, following their behavior from a thin, surface-mode-dominated to a thick, zero-sound-dominated system. Exploring the continuum states they found some well-defined modes and, in particular, identified a nearly momentum-independent mode describing a transverse oscillation of the different layers with respect to each other. Moreover, they analyzed the dynamic structure function $S(q,\hbar\omega)$. This kind of film has been also studied in subsequent works reported by Clements *et al.*,[15,16] where a formalism for the excitation spectrum within a generalized Feynman theory with time-dependent pair correlations was developed and the structures of film layers were compared with two- and three-dimensional (2D and 3D) homogeneous liquids. It is important to notice that in all the above-mentioned CBF studies the excitation energy at large values of q and, in particular, at the roton minimum is too high. On the basis of results obtained for the phonon-roton excitation spectrum of a bulk liquid ^{4}He at $T=0$ K (see Fig. 15 in Ref. 36 and Fig. 18 in Ref. 37), one expects that the inclusion of higher-order correlations[3] and backflow effects[38] will lower the spectrum of an inhomogeneous system and, therefore, it should be considered for any future theoretical improvement.

The aim of the present work is to study elementary excitations for $q>0$, since the long-wavelength limit has been already treated elsewhere.[21] For our investigation we have chosen symmetric finite-width films supported by simple Gaussian-type potentials already adopted in previous papers.[17–21] Although this kind of potential is somewhat unrealistic, the behavior of films confined by them deserves attention. These idealistic systems do not exhibit a layered pattern, but resemble characteristics of the semi-infinite helium discussed in Refs. 22,24. Nevertheless, since they are indeed finite films, a manifestation of film properties is also to be expected, so that it is reasonable to undertake the analysis of these systems awaiting meaningful information to be compared with that obtained from studies of layered films.[13,15,16] From such a comparison it might be possible to isolate and recognize features independent of layered structures. Hence, in order to gain some useful piece of knowledge we carried out a detailed microscopic calculation of excitations in symmetric finite-width films embedded in Gaussian potentials. The evaluations were performed over a large domain of momenta, i.e., $0 < q \leqslant 4$ Å^{-1}. A comprehensive analysis of the excitation energy spectrum $\hbar\omega_\kappa(q)$, the penetration factor $F_\kappa(q)$, the particle-hole energies $V_\kappa(q)$ and $V_\kappa^\dagger(q)$, and the liquid structure factors $S(q,\hbar\omega)$ and $S(q)$ is reported. Among the obtained results, we would like to emphasize the fundamental role of the hardest ''resonant'' state already identified in our previous work (cf. Figs. 4 and 5 in Ref. 19), which for atomic wavelengths can be associated with the ''bulk'' excitations of the film. This state provides the dominant contribution to the static structure function $S(q)$ for 1.2 Å$^{-1} < q < q_R$. In this momentum region there are some crossings and repulsions between bound states, which are examined in detail. In particular, we analyze the connection of our results with the phenomenon discussed by Pitaevskii and Stringari.[35] Another very encouraging result is the successful qualitative interpretation of the experimental data of $S(q,\hbar\omega)$ reported in Ref. 28.

The procedure to obtain the ground state of a Bose many-body problem for a planar symmetry at $T=0$ within CBF theory is outlined in Sec. II. The equations for the elementary excitations are summarized in Sec. III, where the main properties of the eigenvalue problems formulated within both the paired-phonon analysis (PPA) procedure and the generalized Feynman relations are discussed. In this section we also give the formulas needed for the evaluation of the dynamic and static liquid structure functions. In Sec. IV we illustrate the findings of this paper, showing results corresponding primarily to a symmetric film of coverage $n_c = 0.4$ Å^{-2}. Elementary excitations are obtained by solving eigenvalue problems for optimal long-ranged two-body correlation factors deter-

mined in our previous papers.[19–21] In the present work we shall still ignore higher-order correlations and backflow effects. Finally, a summary of all the results is presented in Sec. V.

II. CBF FORMALISM FOR THE GROUND STATE

The physical behavior of an interacting N-body quantum system embedded in an external one-body field is determined by the Hamiltonian

$$H=\sum_{i=1}^{N}\left[-\frac{\hbar^2}{2m}\nabla_i^2+U_{\rm ext}(\mathbf{r}_i)\right]+\sum_{\substack{i,j=1\\(i<j)}}^{N}v(r_{ij}), \qquad (2.1)$$

where $U_{\rm ext}(\mathbf{r}_i)$ is an external one-body potential and $v(r_{ij}=|\mathbf{r}_i-\mathbf{r}_j|)$ a two-body potential which describes the bare interaction between a pair of helium atoms. Effects due to three-body potentials are usually neglected. In the case of a planar geometry, the system is translationally invariant in the x-y plane and symmetry is broken in the z direction, giving rise to a surface structure. This may be due to the action of an external potential of the form $U_{\rm ext}(\mathbf{r}_i)=U_{\rm ext}(z_i)$. Accordingly, any one-body quantity becomes a one-dimensional function, $f_1(\mathbf{r}_i)=f_1(z_i)$, depending only upon the z_i coordinate which is the position of the atom i with respect to a fixed x-y plane. Furthermore, any two-body quantity $f_2(\mathbf{r}_i,\mathbf{r}_j)$ depends only on three variables: (i) the z coordinate of each of the two particles, i.e., z_i and z_j, and (ii) the distance between both particles $|\mathbf{r}_j-\mathbf{r}_i|$ projected onto the x-y plane, i.e.,

$$\eta_{ij}=|\boldsymbol{\eta}_{ij}|=|\boldsymbol{\eta}_j-\boldsymbol{\eta}_i|=\sqrt{(x_j-x_i)^2+(y_j-y_i)^2}. \qquad (2.2)$$

Hence, all two-body quantities can be written as $f_2(\eta_{ij},z_i,z_j)$. Taking into account this simplification a trial N-body wave function for the ground state can be represented by the variational ansatz

$$\Psi_0(1,\ldots,N)=\exp\left[\frac{1}{2}\sum_{i=1}^{N}u_1(z_i)+\frac{1}{2}\sum_{\substack{i,j=1\\(i<j)}}^{N}u_2(\eta_{ij},z_i,z_j)+\cdots\right]. \qquad (2.3)$$

Here $u_1(z_i)$ and $u_2(\eta_{ij},z_i,z_j)$ are, respectively, the one- and two-body correlation factors. In (2.3) correlation factors of more than two particles are neglected.

The optimal values of the correlation factors contributing to the wave function (2.3) should be determined from the Euler-Lagrange (EL) equations derived by minimizing the energy expectation value

$$H_{00}[u_1,u_2]=\frac{\int d^3\mathbf{r}_1\ldots d^3\mathbf{r}_N\Psi_0(\mathbf{r}_1,\ldots,\mathbf{r}_N)H\Psi_0(\mathbf{r}_1,\ldots,\mathbf{r}_N)}{\int d^3\mathbf{r}_1\ldots d^3\mathbf{r}_N\Psi_0^2(\mathbf{r}_1,\ldots,\mathbf{r}_N)}, \qquad (2.4)$$

with respect to both these one- and two-body quantities, i.e., by imposing simultaneously

$$\frac{\delta H_{00}[u_1,u_2]}{\delta u_1}=0 \quad\text{and}\quad \frac{\delta H_{00}[u_1,u_2]}{\delta u_2}=0. \qquad (2.5)$$

In practice, however, in order to derive the EL equations it is convenient to eliminate $u_1(z_i)$ from the energy expectation value in favor of the one-body density $\rho(z_i)$ and the two-body distribution function $g(\eta_{ij},z_i,z_j)$ by using the Bogoliubov-Born-Green-Kirkwood-Yvon equation [for instance, cf. (2.5) in Ref. 17]. The hypernetted-chain (HNC) approximation yields to a set of coupled equations which relate $u(\eta,z_i,z_j)$ and $g(\eta,z_i,z_j)$ (from now on we simplify the notation dropping the index 2, which indicates two-body functions, and setting $\eta\equiv\eta_{ij}$). When all elementary diagrams are neglected this approach (denoted as HNC/0) leads to the hypernetted equation

$$g(\eta,z_1,z_2)=\exp[u(\eta,z_1,z_2)+N(\eta,z_1,z_2)] \qquad (2.6)$$

and the Ornstein-Zernike[39,40] chain equation, which may be conveniently written in momentum space as

$$N(q,z_1,z_2)=\int_{-\infty}^{\infty}dz_3[X(q,z_1,z_2)+N(q,z_1,z_2)]X(q,z_3,z_2), \qquad (2.7)$$

where

$$X(\eta,z_1,z_2)\equiv g(\eta,z_1,z_2)-1-N(\eta,z_1,z_2). \qquad (2.8)$$

Here the auxiliary two-body functions $N(\eta,z_1,z_2)$ and $X(\eta,z_1,z_2)$ are the total and direct (non-nodal) correlations, respectively. Any two-body quantity $f(q,z_1,z_2)$ is the Hankel transform of the corresponding $f(\eta,z_1,z_2)$ evaluated according to

$$\begin{aligned}f(q,z_1,z_2)&=\sqrt{\rho(z_1)\rho(z_2)}\int f(\eta,z_1,z_2)\exp[i(q_xx+q_yy)]dxdy\\&=2\pi\sqrt{\rho(z_1)\rho(z_2)}\int_0^{\infty}\eta d\eta J_0(\eta q)\times f(\eta,z_1,z_2),\end{aligned} \qquad (2.9)$$

wherein J_0 is the zeroth-order Bessel function of the first kind.

A. Optimization equations

The EL equation for $n=1$ is derived from (2.5) with the constraint of a fixed particle number per unit area n_c, sometimes denoted as coverage, defined by

$$n_c=\int_{-\infty}^{\infty}\rho(z)dz. \qquad (2.10)$$

This procedure leads to a Hartree-like equation for the square root of the one-body density:

$$\left[-\frac{\hbar^2}{2m}\frac{d^2}{dz^2}+U_{\rm ext}(z)+V_H(z)\right]\sqrt{\rho(z)}=\mu\sqrt{\rho(z)}, \qquad (2.11)$$

where μ is the chemical potential and $V_H(z)$ is the generalized Hartree potential defined in the Appendix.

On the other hand, the EL equation derived from (2.5) for $n=2$ within the PPA procedure gives an optimization equation for the non-nodal correlation $X(q,z_1,z_2)$:

$$-[H(q,z_1)+H(q,z_2)]X(q,z_1,z_2)+\int_{-\infty}^{\infty}dz_3X(q,z_1,z_3)H(q,z_3)X(q,z_3,z_2)=2\,V_{p\text{-}h}(q,z_1,z_2). \tag{2.12}$$

Here, $H(q,z)$ is a single-particle differential operator defined by

$$H(q,z)=\frac{\hbar^2}{2m}\left[q^2-\frac{1}{\sqrt{\rho(z)}}\frac{d}{dz}\rho(z)\frac{d}{dz}\frac{1}{\sqrt{\rho(z)}}\right]=\epsilon_0(q)+H_0(z), \tag{2.13}$$

where $\epsilon_0(q)=\hbar^2q^2/2m$ is the kinetic energy of a free ^{4}He atom with momentum $\hbar\mathbf{q}$ parallel to the x-y plane, and $V_{p\text{-}h}(q,z_1,z_2)$ is the Hankel transform of the particle-hole potential $V_{p\text{-}h}(\eta,z_1,z_2)$ introduced in Ref. 6 and defined in the Appendix.

B. Optimization procedure

Solutions of the whole EL-HNC/0 problem must be found by solving self-consistently the chain relation (2.7), the Hartree equation (2.11), and the PPA condition (2.12). Equation (2.7) may be solved by either iteration or matrix inversion. The solution of (2.11) can be easily found by using the Newton-Raphson method. The evaluation of the two-body correlation factors is the most cumbersome task and, indeed, it has been the main difficulty for solving inhomogeneous systems in the past. In order to calculate the optimal two-body correlation factor, $u(\eta,z_1,z_2)$, we developed an algorithm[17] which follows as close as possible the procedure devised by Feenberg[3] and Campbell[41] for treating the uniform liquid. Thus we asserted the decomposition

$$u(\eta,z_1,z_2)=u_{\mathrm{SR}}(\eta,z_1,z_2)+\Delta u(\eta,z_1,z_2), \tag{2.14}$$

where the short-ranged correlation factor $u_{\mathrm{SR}}(\eta,z_1,z_2)$ was assumed to be of the generalized McMillan-Schiff-Verlet[42,43] type introduced in Ref. 17:

$$u_{\mathrm{SR}}(\eta,z_1,z_2)=-\left(\frac{b_0+b_1\sqrt{\rho(z_1)\rho(z_2)}}{\sqrt{\eta^2+(z_1-z_2)^2}}\right)^5, \tag{2.15}$$

with $b_0=2.8$ Å and $b_1=9.98$ Å^4, while the optimal long-ranged correction $\Delta u(\eta,z_1,z_2)$ remained to be determined from the optimization PPA relation (2.12), where we set

$$X(q,z_1,z_2)=X_{\mathrm{SR}}(q,z_1,z_2)+\Delta u(q,z_1,z_2). \tag{2.16}$$

In practice, the algorithm starts solving the HNC/0 equations for an initial choice of the density profile $\rho(z)$ and the short-ranged two-body correlation factor $u_{\mathrm{SR}}(\eta,z_1,z_2)$ given by (2.15). Next, the density profile is improved by solving the Hartree equation. This procedure is continued until (2.7) and (2.11) are solved self-consistently. Then, the finite-difference relaxation method proposed in Ref. 17 is applied to get the first long-ranged correction $\Delta u^{(1)}(q,z_1,z_2)$ from the PPA equation (2.12). The new correlation factor $u^{(1)}(\eta,z_1,z_2)=u_{\mathrm{SR}}(\eta,z_1,z_2)+\Delta u^{(1)}(\eta,z_1,z_2)$ is used to solve self-consistently the HNC/0 and Hartree equations. Subsequently, a second correction $\Delta u^{(2)}(q,z_1,z_2)$ is determined from (2.12) and it is used to update the one-body density and the two-body distribution functions by solving, once more, self-consistently Eqs. (2.7) and (2.11). The whole algorithm is iterated until convergence is achieved. We shall not give more details about the method here, since a comprehensive description of it has been very recently reported in Ref. 22.

III. EXCITATION SPECTRUM WITHIN THE CBF FORMALISM

The excitation spectrum of an inhomogeneous Bose fluid with planar symmetry, $\hbar\omega_\kappa(q)$, is determined by an equation of the Bogoliubov type derived in Ref. 6 within the framework of the PPA:

$$H^2(q,z_1)\psi_\kappa(q,z_1)+2\int_{-\infty}^{\infty}dz_2V_{p\text{-}h}(q,z_1,z_2)H(q,z_2)\psi_\kappa(q,z_2)=\hbar^2\omega_\kappa^2(q)\psi_\kappa(q,z_1). \tag{3.1}$$

The quantum number κ may indicate a bound state (by an integer) or it may be a continuous number characterizing the associated energy to continuum states with a nonzero amplitude at very large $|z|$. It can be demonstrated that $\psi_\kappa(q,z)$ are orthogonal in the metric $H(q,z)$, obeying

$$\langle\psi_\kappa(q,z)|H(q,z)|\psi_\nu(q,z)\rangle=\int_{-\infty}^{\infty}dz\,\psi_\kappa(q,z)H(q,z)\psi_\nu(q,z)=e_\kappa(q)\,\delta_{\kappa\nu}. \tag{3.2}$$

It is useful to consider the adjoint eigenvalue equation to (3.1) introduced in Ref. 17, which may be obtained by multiplying (3.1) from the left by $H(q,z_1)$ and redefining the terms

$$H^2(q,z_1)\psi_\kappa^\dagger(q,z_1)+2\int_{-\infty}^{\infty}dz_2[H(q,z_1)V_{p\text{-}h}(q,z_1,z_2)]\psi_\kappa^\dagger(q,z_2)=\hbar^2\omega_\kappa^2(q)\psi_\kappa^\dagger(q,z_1), \tag{3.3}$$

where

$$\psi_\kappa^\dagger(q,z)=a_\kappa(q)H(q,z)\psi_\kappa(q,z). \tag{3.4}$$

It is straightforward to show that (3.1) and (3.3) have both the same spectrum of eigenvalues. An important feature of (3.3) is that the eingenfunctions $\psi_\kappa^\dagger(q,z)$ can be identified with the spatial shapes of the normal modes defined in Refs. 6,7. A generalized orthonormalization integral may be written as

$$\langle\psi_\kappa(q,z)|\psi_\nu^\dagger(q,z)\rangle=\int_{-\infty}^{\infty}dz\,\psi_\kappa(q,z)\psi_\nu^\dagger(q,z)=a_\nu(q)\langle\psi_\kappa(q,z)|H(q,z)|\psi_\nu(q,z)\rangle$$

$$=a_\kappa(q)e_\kappa(q)\delta_{\kappa\nu}=N_\kappa(q)\delta_{\kappa\nu}, \tag{3.5}$$

so that we are dealing with two families of eigenfunctions, which are orthogonal to one another according to (3.5). Therefore, there are two sets of normalization factors, one for each family, which may be chosen depending on the system to be studied. Although the actual values of $e_\kappa(q)$ and $a_\kappa(q)$ do depend on the normalization choices, the physical observables are independent of them.

A. Nature of the eigenstates

In the present paper the spectrum of elementary excitations was determined from the eigenvalue problems (3.1) and (3.3). Solutions of these dispersion relations provide bound and continuum states.[30–32] Furthermore, according to the discussions of Refs. 10,13,22,24,25 energies $\hbar\omega_\kappa(q)$ of bound states should be lower than the separation energy $\epsilon_S(q)$ corresponding to the emission of a free ^{4}He atom into a vacuum:

$$\hbar\omega_\kappa(q)<\epsilon_S(q)=-\mu+\epsilon_0(q). \tag{3.6}$$

The number of bound states depends on the particular characteristics of the system which is analyzed. In general, there may be one or more of these states which form a discrete spectrum restricted to have energies smaller than $\epsilon_S(q)$ and on top of this upper limit the continuous spectrum is built.

The usual way to obtain the excitation energies and the corresponding eigenfunctions numerically is to discretize Eqs. (3.1) and (3.3) for a fixed value of q on a finite mesh over the z_1-z_2 plane. Such a procedure will, of course, only provide discrete states and, in particular, a discrete subset of the continuum states. In practice, since the long-range behavior of functions appearing in the kernels of these equations is known, it is possible to get a better representation of the continuous spectrum by extending the mesh to larger box sizes. This improvement provides a denser spectrum from which reliable information on physical observables can be extracted.

When treating finite-size films it is convenient to normalize both kinds of eigenfunctions to unity, i.e.,

$$\langle\psi_\kappa(q,z)|\psi_\kappa(q,z)\rangle=\int_{-\infty}^{\infty}dz\,\psi_\kappa^2(q,z)=1 \tag{3.7}$$

and

$$\langle\psi_\kappa^\dagger(q,z)|\psi_\kappa^\dagger(q,z)\rangle=1. \tag{3.8}$$

Using this normalization, the expectation value of the one-body operator $H(q,z)$ defined in (3.2) may be cast, after a straightforward algebra, into the suitable form

$$e_\kappa(q)=\epsilon_0(q)+\frac{\hbar^2}{2m}\int_{-\infty}^{\infty}dz\rho(z)\left[\frac{d}{dz}\frac{\psi_\kappa(q,z)}{\sqrt{\rho(z)}}\right]^2. \tag{3.9}$$

Furthermore, it is also useful to define the adjoint expectation value

$$e_\kappa^\dagger(q)=\langle\psi_\kappa^\dagger(q,z)|H(q,z)|\psi_\kappa^\dagger(q,z)\rangle=\epsilon_0(q)+\frac{\hbar^2}{2m}\int_{-\infty}^{\infty}dz\rho(z)\left[\frac{d}{dz}\frac{\psi_\kappa^\dagger(q,z)}{\sqrt{\rho(z)}}\right]^2. \tag{3.10}$$

An expression for the eigenvalues can be derived from (3.3) by multiplying from the left by $\psi_\kappa(q,z_1)$ and integrating over z_1,

$$\hbar^2\omega_\kappa^2(q)\int_{-\infty}^{\infty}dz_1\psi_\kappa(q,z_1)\psi_\kappa^\dagger(q,z_1)=\int_{-\infty}^{\infty}dz_1\psi_\kappa(q,z_1)H^2(q,z_1)\psi_\kappa^\dagger(q,z_1)$$
$$+2\int_{-\infty}^{\infty}\int_{-\infty}^{\infty}dz_1dz_2\psi_\kappa(q,z_1)[H(q,z_1)V_{p\text{-}h}(q,z_1,z_2)]\psi_\kappa^\dagger(q,z_2), \tag{3.11}$$

which may be cast in a more compact form

$$\hbar^2\omega_\kappa^2(q)=\frac{e_\kappa(q)}{N_\kappa^2(q)}\left[\int_{-\infty}^{\infty}dz_1\psi_\kappa^\dagger(q,z_1)H(q,z_1)\psi_\kappa^\dagger(q,z_1)+2\int_{-\infty}^{\infty}\int_{-\infty}^{\infty}dz_1dz_2\psi_\kappa^\dagger(q,z_1)V_{p\text{-}h}(q,z_1,z_2)\psi_\kappa^\dagger(q,z_2)\right]$$
$$=\frac{e_\kappa(q)[e_\kappa^\dagger(q)+2V_\kappa^\dagger(q)]}{N_\kappa^2(q)}=\frac{e_\kappa(q)}{N_\kappa^2(q)}h_\kappa^\dagger(q). \tag{3.12}$$

B. Expressions for liquid structure factors

As mentioned in the Introduction, an interesting issue is to establish at which values of q the different kind of solutions described above yield sizable contributions to the static structure factor $S(q)$. This quantity is defined as

$$S(q)=\sum_{\hbar\omega}S(q,\hbar\omega), \tag{3.13}$$

where $S(q,\hbar\omega)$ is the diagonal dynamic structure function and the sum runs over bound and continuum states of the eigenvalue problem (3.3). However, since we have discretized the equations, the summation runs over bound states and a discrete set representing the continuous spectrum. According to (4.4) of Ref. 13 we have

$$S(q,\hbar\omega)=\int_{-\infty}^{\infty}\int_{-\infty}^{\infty}dz_1dz_2\sqrt{\frac{\rho(z_1)}{n_c}}\sqrt{\frac{\rho(z_2)}{n_c}}\int d^2\boldsymbol{\eta}e^{i\mathbf{q}\cdot\boldsymbol{\eta}}S(\mathbf{r}_1,\mathbf{r}_2,\hbar\omega), \tag{3.14}$$

with

$$\int d^2\boldsymbol{\eta}e^{i\mathbf{q}\cdot\boldsymbol{\eta}}S(\mathbf{r}_1,\mathbf{r}_2,\hbar\omega)=\frac{e_\kappa(q)}{\hbar\omega_\kappa(q)N_\kappa^2(q)}\psi_\kappa^\dagger(q,z_1)\psi_\kappa^\dagger(q,z_2), \tag{3.15}$$

where κ stands for bound states and the discretized subset of the continuum states $\hbar\omega$ introduced by our procedure. Therefore within the framework of this normal-mode decomposition we arrive at

$$S(q,\hbar\omega)=\frac{e_\kappa(q)}{\hbar\omega_\kappa(q)N_\kappa^2(q)}\int_{-\infty}^{\infty}\int_{-\infty}^{\infty}dz_1dz_2\sqrt{\frac{\rho(z_1)}{n_c}}\sqrt{\frac{\rho(z_2)}{n_c}}\psi_\kappa^\dagger(q,z_1)\psi_\kappa^\dagger(q,z_2)$$
$$=\frac{1}{\hbar\omega_\kappa(q)}\left[\frac{e_\kappa(q)}{N_\kappa^2(q)}\right]\left[\int_{-\infty}^{\infty}dz\sqrt{\frac{\rho(z)}{n_c}}\psi_\kappa^\dagger(q,z)\right]^2=S_\kappa(q). \tag{3.16}$$

Finally, the static structure function in the parallel direction may be expressed as

$$S(q)=\sum_\kappa S_\kappa(q)=\sum_\kappa\frac{1}{\hbar\omega_\kappa(q)}\left[\frac{e_\kappa(q)}{N_\kappa^2(q)}\right]\left[\int_{-\infty}^{\infty}dz\sqrt{\frac{\rho(z)}{n_c}}\psi_\kappa^\dagger(q,z)\right]^2. \tag{3.17}$$

This form indicates that all addends are positive definite. Furthermore, since $\sqrt{\rho(z)}$ is an even function of z only, even eigenstates $\psi_\kappa^\dagger(q,z)$ will lead to nonzero results for $S_\kappa(q)$. We shall examine in the next section the size of all partial contributions to the expansion for the static structure factor as a function of momentum.

IV. NUMERICAL RESULTS AND ANALYSIS

According to the motivation discussed in the Introduction, we shall report results obtained for elementary excitations of symmetric films confined by a simple external potential $U_{\text{ext}}(z)$ of the form

$$U_{\text{ext}}(z)=-U_2\exp[-z^2/(2s^2)]-U_4\exp[-z^4/(4s^4)]. \tag{4.1}$$

The parameters of this potential were fixed in order to get films with a central density close to the experimental equilibrium density of bulk liquid ^{4}He at $T=0$ K, i.e., $\rho_c\simeq0.0218$ Å^{-3} (see Refs. 19–21). It was assumed that helium atoms interact via the improved Hartree-Fock disper-

sion potential (dubbed HFDHE2) with the parameters determined by Aziz *et al.*[44] The main findings will be illustrated with results for a film of coverage $n_c=0.4$ Å^{-2} confined by $U_{\rm ext}(z)$ with the parameters $U_2=0$, $U_4=12$ K, and $s=6$ Å, although marginally we shall also comment on a film with $n_c=0.3$ Å^{-2} supported by a potential with $U_2=7$ K, $U_4=7$ K, and $s=5$ Å.

A. Classification of states

The complete EL-HNC/0 problem has been solved within a box size ($-z^0_{\rm max}\leqslant z\leqslant z^0_{\rm max}=18.6$ Å). Once having optimized the one-body density $\rho(z)$ and the two-body correlation factor $u(\eta,z_1,z_2)$, dispersion relations were solved to get information about excitations. It is well known that wave functions of bound states must vanish exponentially for $z\to\pm\infty$. Therefore, in order to be sure that numerical calculations have been carried out within a sufficiently large box, we verified that the amplitudes of bound eigenstates decay exhibiting negligible values at $z=\pm z^0_{\rm max}$. The number of bound states depends on the momentum q, the thickness of the system, and the strength and width of the external potential. Furthermore, it was also checked that wave functions corresponding to continuum states approach plane waves within the selected box. These results guarantee that at the boundary all local as well as nonlocal terms in the dispersion relations have already reached their asymptotic values.

In order to get a rather dense subset of continuum states the eigenvalue problems (3.1) and (3.3) were discretized in boxes of size $z_{\rm max}$ larger than $z^0_{\rm max}$ in which the complete numerical EL-HNC/0 task has been performed. For the extended calculations the particle-hole interaction was set to zero outside the region of the original box, i.e., $V_{p\text{-}h}(q,z_1,z_2)=0$ whenever z_1 and/or $z_2>z^0_{\rm max}$. On the other hand, the one-body density was extrapolated to large distances by the known asymptotic form

$$\rho(z)=\begin{cases}\rho(z^0_{\rm max})\exp[-2\sqrt{-2m\mu/\hbar^2}(z-z^0_{\rm max})] & \text{if } z>z^0_{\rm max},\\ \rho(-z^0_{\rm max})\exp[2\sqrt{-2m\mu/\hbar^2}(z+z^0_{\rm max})] & \text{if } z<-z^0_{\rm max}.\end{cases}\tag{4.2}$$

The extended eigenvalue problems were solved by assuming vanishing boundary conditions, i.e.,

$$\psi_\kappa(q,z=\pm z_{\rm max})=\psi^\dagger_\kappa(q,z=\pm z_{\rm max})=0,\tag{4.3}$$

so that we imposed that all wave functions must have a node at the border. This choice is the appropriate one for the continuum states (which become standard standing waves for large z) and, since anyway all bound wave functions have negligible amplitudes for $|z|>z^0_{\rm max}$, we are not losing any information about them due to the condition (4.3).

In practice, instead of calculating only one spectrum for a rather large box, we evaluated a series of spectra by enlarging slowly $z_{\rm max}$. During this procedure we followed the evolution of the obtained eigenstates by looking at their energy and wave function. Of course, as is to be expected in so doing, the energies and wave functions of the bound states do not change. However, to our surprise, we found that there are also continuum states which energy remains constant when the box is enlarged. Figure 1 shows, in the case of the film with coverage $n_c=0.4$ Å^{-2}, the evolution of energy levels of the even eigenstates as a function of box size for two fixed momentum values, namely, at $q=0.1$ and 1.0 Å^{-1}. Energies corresponding to odd eigenstates are not displayed for two reasons: (i) because they do not contribute to physical observables like, for instance, the liquid structure factors and (ii) in order to avoid the overload of plots. This drawing indicates clearly that above the separation energy $\epsilon_S(q)$ there are a few states which energy does not change when $z_{\rm max}$ is increased. The wave functions corresponding to these special continuum states obtained at $q=0.1$ Å^{-1} are shown in Fig. 2, where for the sake of comparison a typical "regular" continuum mode and the lowest-lying eigenfunction for $q=0$, which is nothing but to the normalized square root of the density profile $\psi_0(q=0,z)=\sqrt{\rho(z)/n_c}$, are also plotted. These special wave functions exhibit inside the film enhanced amplitudes which decrease rapidly in the inhomogeneous interface region ($8\leqslant z\leqslant 13$ Å) and show strongly attenuated plane waves in the asymptotic limit. The general features of these modes change very little with momentum up to a value of q around 0.8 Å^{-1}. Beyond this momentum the number of oscillations with large amplitudes becomes smaller. For instance, Fig. 3 shows results obtained at $q=1.3$ Å^{-1}. In this plot, the highest level placed at

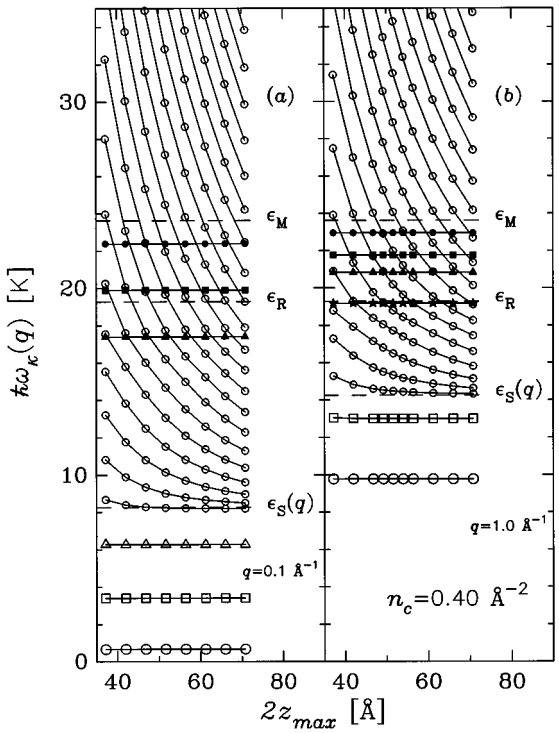

FIG. 1. Evolution of the discretized excitation energy spectrum of the symmetric film of coverage $n_c=0.4$ Å^{-2} as a function of the box size for two fixed values of momentum q. Only energies corresponding to even eigenstates are displayed. In order to have a reference for the continuous spectrum the separation energy $\epsilon_S(q)=-\mu+\epsilon_0(q)$ is indicated. For the sake of comparison the maxon energy ϵ_M and the roton energy ϵ_R both of them evaluated for a bulk liquid at a density of $\rho_L=0.0218$ Å^{-3} are also plotted. (a) Data calculated at $q=0.1$ Å^{-1}. (b) Same as (a) at $q=1.0$ Å^{-1}.

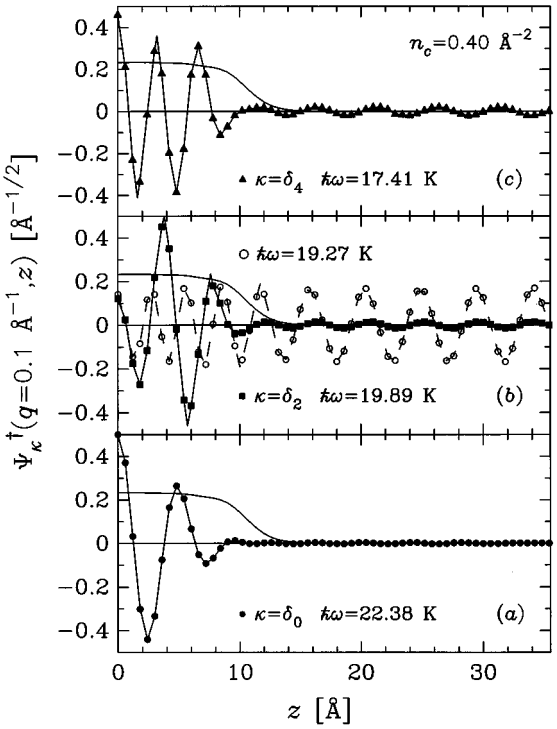

FIG. 2. The δ_0, δ_2, and δ_4 ''resonant modes'' at $\hbar\omega=22.38$, 19.89, and 17.41 K obtained in the case of coverage $n_c=0.4$ Å^{-2} for $q=0.1$ Å^{-1} together with a typical ''regular'' continuum mode at $\hbar\omega=19.27$ K. For comparison the solid curve indicates the normalized square root of the density profile $\psi_0(q=0,z)=\sqrt{\rho(z)/n_c}$. All these quantities are symmetric at $z=0$.

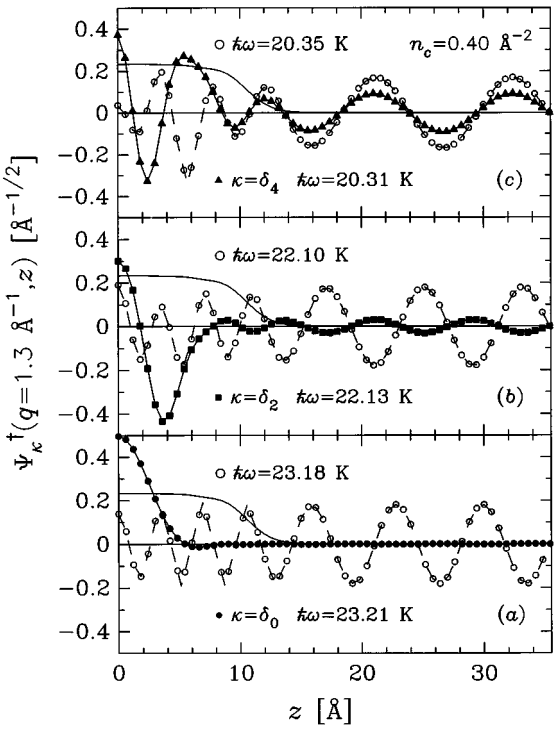

FIG. 3. The δ_0, δ_2, and δ_4 ''resonant modes'' at $\hbar\omega=23.21$, 22.13, and 20.31 K obtained in the case of coverage $n_c=0.4$ Å^{-2} for $q=1.3$ Å^{-1} together with neighboring ''regular'' continuum modes at $\hbar\omega=23.18$, 22.10, and 20.35 K. For comparison the solid curve indicates the normalized square root of the density profile $\psi_0(q=0,z)=\sqrt{\rho(z)/n_c}$. All these quantities are symmetric at $z=0$.

$\hbar\omega=23.21$ K develops only one large amplitude and its associated plane wave remains almost negligible. The lower special state at $\hbar\omega=22.13$ K presents three large amplitudes within the film domain (note that in Fig. 3 only half of the film is displayed) and a somewhat more intense plane wave than that corresponding to the level at $\hbar\omega=23.21$ K. Finally, the state at $\hbar\omega=20.31$ K develops five large amplitudes and exhibits the biggest plane wave component of all three examined wave functions. Taking into account the properties of these special continuum states described above we shall denote them as ''resonant modes.'' Namely, we shall refer to them as $\kappa=\delta_0$ (for the highest and hardest ''resonant mode''), $\kappa=\delta_2$ (the first lower one), and $\kappa=\delta_4$ (the lowest and softest one). The index n of δ_n is even because we are just treating even eigenstates. As a matter of fact, in a preliminary report we have already identified the $\kappa=\delta_0$ ''resonant mode'' and commented some of its features (cf. Figs. 4 and 5 in Ref. 19). However, since in general the evaluated ''continuum modes.'' are really a superposition of many modes in an energy interval determined by the discretization mesh, at least, a brief clarification should be made about the nature of these ''resonant modes.'' An analysis of their widths indicates that these quantities are confined to very narrow energy bands, much smaller than the typical distance between two consecutive ''regular'' continuum solutions. For instance, Fig. 3 shows that in the neighborhood of all these special states there are levels which lying at a distance of only $\Delta\hbar\omega\approx0.03$ K already exhibit the behavior of the ''regular'' continuum. Therefore, due to the fact that their energies are very well defined one can indeed speak of ''resonant modes.''

B. Excitation energy spectrum

Let us as now analyze the excitation spectrum as a function of momentum q. Figures 4 and 5 show the energies of the even eigenstates obtained from the dispersion relations (3.1) and (3.3) in the case of two different coverages $n_c=0.4$ and 0.3 Å^{-2}, respectively. To guide the eye when looking at these figures, several additional curves are also plotted: the separation energy $\epsilon_S(q)$ given by (3.6); the Bijl-Feynman dispersion relation for bulk liquid ^{4}He,

$$\hbar\omega_L(q)=\epsilon_L(q)=\frac{\hbar^2q^2}{2mS_L(q)}=\frac{\epsilon_0(q)}{S_L(q)}, \tag{4.4}$$

evaluated at experimental equilibrium density $\rho_L=0.0218$ Å^{-3}; and two horizontal straight lines representing the maxon energy ϵ_M and the roton energy ϵ_R of the bulk system. Of course, the results provided by (3.1) and (3.3) are coincident. A comparison of these drawings indicates a similar general behavior; however, there are some differences.

In the case of $n_c=0.3$ Å^{-2} the three lowest-lying levels are always bound, whereas for $n_c=0.4$ Å^{-2} there are only two states of this kind. Note that the third bound level present in Fig. 4 at small momenta merges into the continuum at $q\approx0.5$ Å^{-1}. Furthermore, in both figures a barely

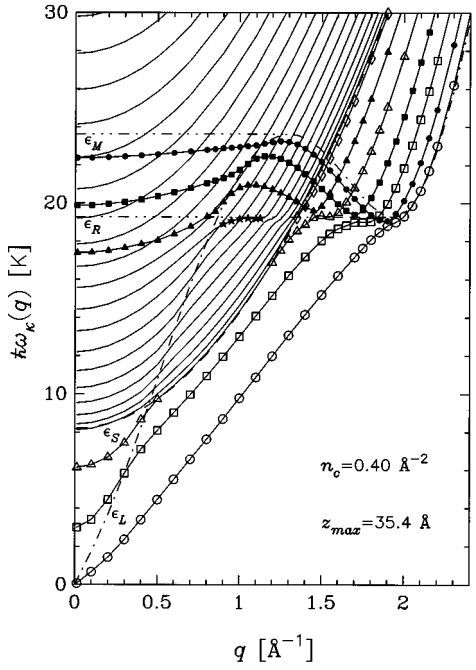

FIG. 4. Excitation spectrum of even eigenstates as a function of momentum for the film of coverage $n_c=0.4$ Å^{-2}. The open symbols ○, □, △, and ◇ stand for bound states, which are surface excitations for $\hbar\omega_\kappa(q)<\epsilon_R$. The excitation energies of "resonant modes" like those examined in Figs. 2 and 3 are pointed out by full symbols. The ● represents the highest "resonant mode." The solid curves without any particular mark indicate energies of the discretized "regular" continuum modes. The dashed line is the separation energy $\epsilon_S(q)$ being the upper limit for discrete eigenvalues. The dot-dashed line is the dispersion relation $\epsilon_L(q)$ for a uniform system, while the horizontal dot-dot-dot-dashed lines are the maxon energy $\epsilon_M\approx 23.6$ K and the roton energy $\epsilon_R\approx 19.3$ K; all of them were evaluated for a bulk liquid at a density of $\rho_L=0.0218$ Å^{-3}.

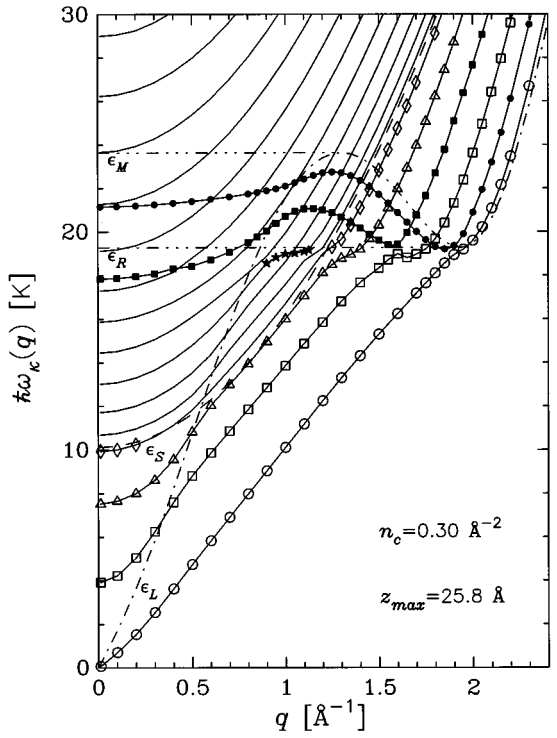

FIG. 5. Same as Fig. 4 for the film of coverage $n_c=0.3$ Å^{-2}.

bound level at $\hbar\omega\approx-\mu$ for $q\leqslant 0.2$ Å^{-1} appears; however, in particular for $n_c=0.4$ Å^{-2} due to numerical uncertainties, it becomes very difficult to disentangle whether it is really the fourth bound state. For both coverages the first- and second-lowest modes are clearly surface excitations up to the roton minimum. Their wave functions are very similar to that obtained when studying a semi-infinite system; see Figs. 4, 5, and 6 in Ref. 22. Here we shall restrict ourselves to show in Fig. 6(a) the spatial shape of the lowest-lying excitation, normally identified with the ripplon, calculated for $n_c=0.4$ Å^{-2} at values of q shortly below the momentum corresponding to the roton minimum, $q_R\approx 1.9$ Å^{-1}. We display these results because they will be needed for a forthcoming discussion. Above the separation energy a discrete set of states representing the continuous spectrum is mounted. The energies of the "regular" continuum indicated by solid curves build a sequence of levels almost parallel to $\epsilon_S(q)$. On the other hand, the excitation energies of "resonant modes" like those examined in Figs. 2 and 3 are indicated by solid symbols (circles, squares, and triangles). There are three of the latter kind of modes in Fig. 4 and two in Fig. 5. The energies of these modes vary slowly up to the maxon domain, and then rise more pronouncedly, reaching a maximum in the interval $1.05\leqslant q\leqslant 1.25$ Å^{-1}, and subsequently fall approaching the area of the roton minimum, $\epsilon_R\approx 19.3$ K, by following a curve approximately parallel to $\hbar\omega_L(q)$. The behavior after the crossing with the separation energy $\epsilon_S(q)$ is very interesting and will be analyzed in detail in the next paragraph. Another feature worthy of being pointed out is the appearance of a further "resonant mode" at $q\approx 0.9$ Å^{-1} in both Figs. 4 and 5, which energies are a bit smaller than the roton energy ϵ_R. This mode merges into the "regular" continuum at about $q\approx 1.15$ Å^{-1}.

Let us now focus our attention on the analysis of the film of coverage $n_c=0.4$ Å^{-2}. In Fig. 4, for $q>1.35$ Å^{-1} and below the separation energy, besides several level crossings there are three level repulsions. These features may be observed better in Fig. 7 which shows an amplification of the region to be explored. First of all, notice the appearance of a third bound state at $q\approx 1.35$ Å^{-1} and of a fourth one at $q\approx 1.4$ Å^{-1}. Figure 7 indicates that the "resonant modes" first cross "regular" continuum modes above the separation energy, and then become bound below $\epsilon_S(q)$ and continue the fall until are repelled by lower-lying surface modes with a similar number of large amplitudes. The first level repulsion occurs at $q\approx 1.5$ Å^{-1} between the $\kappa=4$ elementary excitation and the bound continuation of the $\kappa=\delta_4$ "resonant mode," the second one takes place at $q\approx 1.7$ Å^{-1} between the $\kappa=2$ surface excitation and the bound continuation of the $\kappa=\delta_2$ "resonant mode," and finally the bound continuation of the $\kappa=\delta_0$ "resonant mode" is repelled by the $\kappa=0$ ripplon excitation at $q\approx 1.9$ Å^{-1}. All these results provide evidence for the existence of a sort of repulsive interaction between the approaching levels around $\hbar\omega\approx\epsilon_R$ in agreement with the suggestion of Pitaevskii and Stringari.[35]

In the momentum region of the repulsions, due to the strong interaction between eigenstates, the character of the corresponding wave functions is changed. The clearest trans-

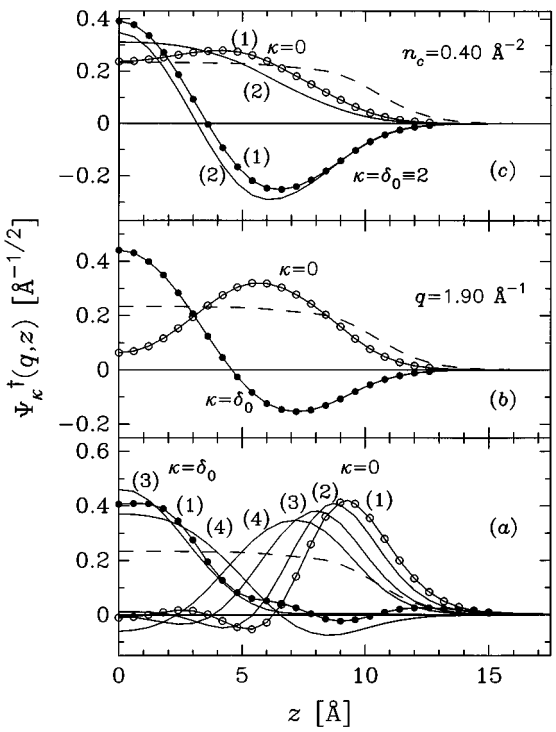

FIG. 6. The lowest-lying $\kappa=0$ excitation and the δ_0 ''resonant mode'' as a function of z at momenta close to the roton minimum $q_R\approx 1.9$ Å^{-1}. The dashed curve is the normalized square root of the density profile $\psi_0(q=0,z)=\sqrt{\rho(z)/n_c}$. (a) Curves (1), (2), (3), and (4) correspond, in turn, to $q=1.6$, 1.7, 1.8, and 1.85 Å^{-1}. (b) Both these wave function at $q=1.9$ Å^{-1}. (c) Curves (1) and (2) correspond, in turn, to $q=1.925$ and 1.95 Å^{-1}. All these quantities are symmetric at $z=0$.

formation of the character of excitation modes happens when the $\kappa=0$ and the bound continuation of the $\kappa=\delta_0$ approach one another; therefore we concentrate our discussion on this case. The situation is documented in Fig. 6, which shows these wave functions shortly below and shortly above the level repulsion at $q\approx 1.9$ Å^{-1}. Figure 7 indicates that for $q>1.8$ Å^{-1} these modes are the first- and second-lowest even excitations. From Fig. 6 it is obvious that during the approach the geometric shape of the wave functions changes continuously in such a way that after the repulsion none of these modes is a surface excitation any more. As shown in Fig. 6(c) for $q\geqslant 1.95$ Å^{-1} the lowest-lying and the first-excited even state exhibit the behavior of typical nodeless

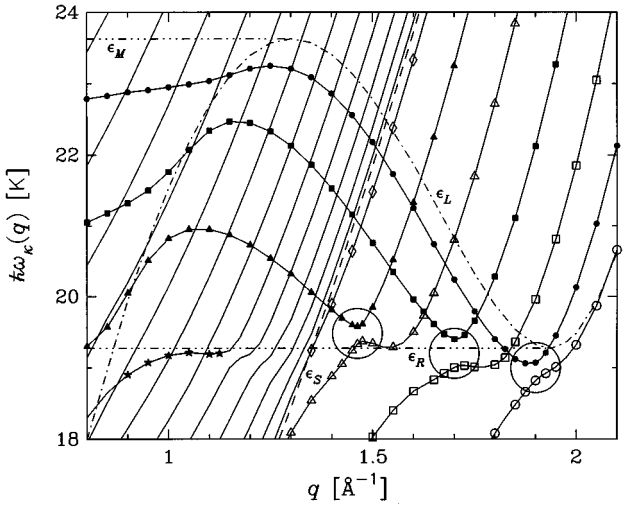

FIG. 7. Same as Fig. 4 for the maxon-roton region. The big circles indicate the region where repulsions of states take place.

and two-node volume wave functions, respectively. Similar features to that displayed in Fig. 6 also occur close to the other repulsions at $q\approx 1.5$ and 1.7 Å^{-1}. Moreover, the same kind of repulsions is also present in the energy spectrum corresponding to the thinner film of coverage $n_c=0.3$ Å^{-2} shown in Fig. 5.

On the other hand, turning now to both Figs. 4 and 5, it may be seen that shortly after the repulsions all excitation energies become nearly parallel to the separation line $\epsilon_S(q)$; i.e., they depend to a good approximation quadratically on q in that momentum regime. As a matter of fact, for $q>1.5$ Å^{-1} in the region delimited from above by the separation line $\epsilon_S(q)$ and from below by the curve $\epsilon_L(q)$, that is, when the excitation energies cross the bulk result after all rearrangements, it is then convenient to make a new identification of these bound wave functions, characterizing them by integral numbers κ which indicate the number of nodes.

C. Particle-hole matrix elements

To learn something more about the properties of the ''resonant modes'' we have analyzed the expectation values (3.12) making a contact with excitations of bulk liquid. In this part of the investigation we shall proceed in a similar manner as Gernoth *et al.*[22] studied the semi-infinite system. Accordingly, we cast the dispersion relation (3.12) into the form given by Eq. (35) of Ref. 22:

$$\hbar^2\omega_\kappa^2(q)=\frac{e_\kappa(q)}{N_\kappa^2(q)}[e_\kappa^\dagger(q)+2V_\kappa^\dagger(q)]=\frac{F_\kappa(q)}{q}\epsilon_0(q)[e_\kappa^\dagger(q)+2V_\kappa^\dagger(q)], \tag{4.5}$$

where $F_\kappa(q)$ is the penetration factor,

$$F_\kappa(q)=\frac{q}{\epsilon_0(q)}\times\frac{e_\kappa(q)}{N_\kappa^2(q)}. \tag{4.6}$$

It is worth mentioning that for $\kappa=0$ the relation (4.5) provides a useful stability condition on the elementary excitations [see discussion of Eq. (3.8) in Ref. 17]. The energy expression (4.5) is an analog of the familiar dispersion relation of the elementary excitations in bulk liquid ^{4}He described by plane waves:[2,3]

$$\epsilon_L^2(q)=\epsilon_0(q)[\epsilon_0(q)+2V_L(q)], \tag{4.7}$$

where the quantity $V_L(q)$ is the 3D Fourier transform of the isotropic particle-hole potential at density ρ_L. Remember that for a uniform system the penetration factor is $F_L(q)=q$. Moreover, for optimized solutions expression (4.7) is equivalent to the Bijl-Feynman relation (4.4).

In the case of a half-space system, Gernoth *et al.*[22] found that the penetration factor for ripplon excitations, $F_0(q)$, merges into the bulk factor $F_L(q)$ near the roton momentum q_R (see Fig. 7 therein). Making a connection between this result and the expression (4.6) one may conclude that in this momentum regime the ratio $e_0(q)/N_0^2(q)$ closely approaches the kinetic energy $\epsilon_0(q)$. On the other hand, Fig. 8 in Ref. 22 shows that in the same momentum region $e_0^\dagger(q)$ also tends to $\epsilon_0(q)$. In trying to understand these findings in terms of theoretical expressions, one realizes that neglecting the effects of $H_0(z)$ in (3.2), (3.9), and (3.10) we just get $e_0^\dagger(q)=e_0(q)=\epsilon_0(q)$. In light of this result, we may conjecture that for this class of states the influence of the operator $H_0(z)$ on the wave functions $\psi_0(q,z)$ would become very small. Under such an assumption definition (3.4) yields

$$\psi_0^\dagger(q,z)=a_0(q)H(q,z)\psi_0(q,z)=a_0(q)[\epsilon_0(q)+H_0(z)]\psi_0(q,z)\approx\psi_0(q,z). \tag{4.8}$$

Using this result in (3.5) we obtain that $N_0(q)\approx 1$, which leads to $e_0(q)/N_0^2(q)\approx e_0^\dagger(q)\approx\epsilon_0(q)$. Hence, the result $F_0(q)\approx q$ near q_R can be well understood. In addition, due to the property (4.8), the two different matrix elements of the particle-hole potential, namely, $V_0^\dagger(q)$ and $V_0(q)$, become approximately equal in this momentum regime:

$$\begin{aligned} V_0^\dagger(q)&=\langle\psi_0^\dagger(q,z_1)|V_{p\text{-}h}(q,z_1,z_2)|\psi_0^\dagger(q,z_2)\rangle \\ &\approx\langle\psi_0(q,z_1)|V_{p\text{-}h}(q,z_1,z_2)|\psi_0(q,z_2)\rangle=V_0(q). \end{aligned} \tag{4.9}$$

Then, for the excitation energy of this class of modes we are led to the approximation

$$\hbar^2\omega_0^2(q)\approx\epsilon_0(q)[\epsilon_0(q)+2V_0^\dagger(q)]\approx\epsilon_0(q)[\epsilon_0(q)+2V_0(q)]. \tag{4.10}$$

Of course, a next step in Ref. 22 was to compare the calculated values of the particle-hole energies $V_0^\dagger(q)$ and $V_L(q)$. It is shown in Fig. 11 of Ref. 22 that the surface quantity $V_0^\dagger(q)$ approaches the bulk energy $V_L(q)$ close to q_R. According to Gernoth *et al.*[22] the similarity of the dispersion relations (4.7) and (4.10), on the one hand, and the nature of the results for the driving forces $V_0^\dagger(q)$ and $V_L(q)$, on the other, point to an intimate relation between rotons and the surface modes at large momenta. Since bulk rotons at $q\approx q_R$ respond to the strength $V_L(q)$, while the surface modes at atomic wavelengths are driven by the corresponding surface quantity $V_0^\dagger(q)$, they interpreted these surface modes as rotons trapped in the surface layer.

We performed in the case of symmetric finite-width films a similar analysis to that described above. In Fig. 8 we compare the quantity $V_0^\dagger(q)$ calculated for the symmetric films of coverages $n_c=0.3$ and 0.4 Å^{-2} with the results for the semi-infinite system published in Ref. 22 and the particle-hole energy $V_L(q)$ at a density of $\rho_L=0.0218$ Å^{-3}. The values obtained for the film with $n_c=0.4$ Å^{-2} lie close to those corresponding to the half-space along the whole domain of surface excitations below q_R; furthermore, for momenta larger than q_R these results agree very well with $V_L(q)$. On the other hand, the evaluations for the $n_c=0.3$ Å^{-2} film exhibit larger discrepancies with the half-space values as well as with $V_L(q)$, which indicates that for this thinner film the finite-size effects are still important. Therefore from now on we shall concentrate our discussion on results for the film of coverage $n_c=0.4$ Å^{-2}.

The values of the penetration factors and the particle-hole energies are collected in Figs. 9 and 10, respectively. Our study has not been restricted to the lowest-lying state. We also examined the behavior of the first-excited even state as well as of ''resonant modes'' and their bound continuations. Figure 9 indicates that the penetration factor $F_0(q)$ evaluated in the present work exhibits a behavior similar to that observed in the case of the half-space system. In particular, it also approaches the straight line $F_L(q)=q$ at $q\approx q_R$. On the other hand, $F_{\delta_0}(q)$ is much bigger than $F_L(q)$ for $q\leqslant 1.1$ Å^{-1}, and then it crosses with $F_0(q)$ and approaches the bulk result at $q\approx 1.3$ Å^{-1} lying very close to $F_L(q)$ for $q<q_R$. At $q\approx q_R$ there is a new crossing of $F_{\delta_0}(q)$ with $F_0(q)$, and the latter quantity remains close to $F_L(q)$. As an illustration of the behavior of the penetration factors corresponding to other modes we also plotted in Fig. 9 the data of the pair $F_2(q)$ and $F_{\delta_2}(q)$. The former one grows at small momenta until $q\approx 0.5$ Å^{-1} where it reaches the value $F_2(q)\approx 2$ Å^{-1}; for larger momenta it remains approximately constant up to $q\approx q_R$. The quantity $F_{\delta_2}(q)$ exhibits a behavior resembling that of $F_{\delta_0}(q)$. After starting from large values it decreases abruptly and crosses with $F_2(q)$ at $q\approx 0.9$ Å^{-1}; subsequently, it lies below $F_2(q)$ until a momentum slightly

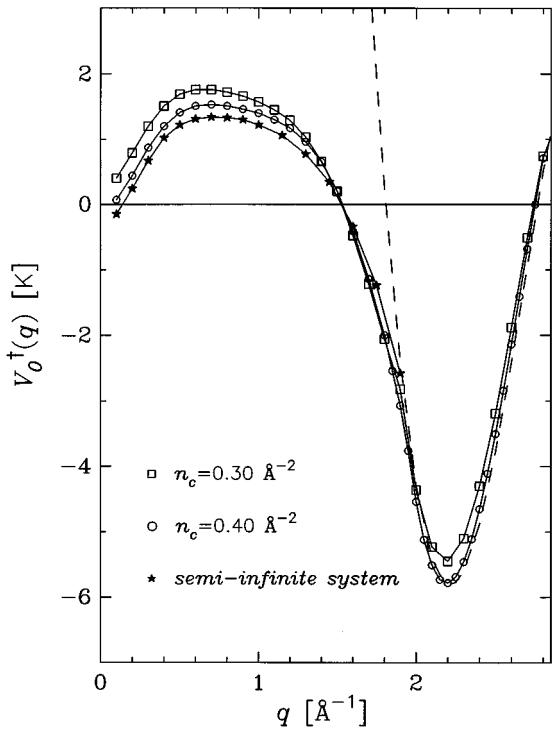

FIG. 8. Particle-hole energies $V_0^\dagger(q)$ plotted against the wave number q. The symbols □ and ○ stand for evaluations performed for films with coverages $n_c=0.3$ and 0.4 Å^{-2}, respectively. The star stands for the expectation value $V_0^\dagger(q)$ obtained in Ref. 22 in the case of the half-space system, whereas the dashed curve indicates the particle-hole energy $V_L(q)$ calculated for a bulk liquid at a density of $\rho_L=0.0218$ Å^{-3}.

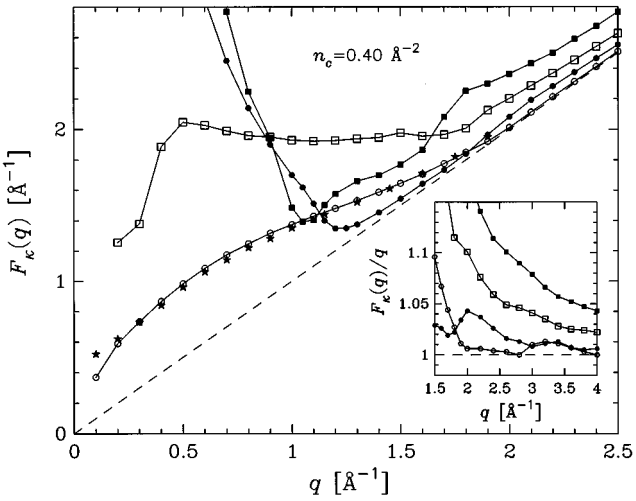

FIG. 9. Penetration factor $F_\kappa(q)$ defined by Eq. (4.6) as a function of the momentum q. The symbols ○ and □ stand, in turn, for $F_0(q)$ and $F_2(q)$, whereas the corresponding solid symbols indicate the results for $F_{\delta_0}(q)$ and $F_{\delta_2}(q)$ and their bound continuations. The star stands for the expectation value $F_0(q)$ obtained in Ref. 22 in the case of the half-space system and the dashed line indicates the bulk penetration factor $F_L(q)=q$. The inset shows the ratio $F_\kappa(q)/q$ for large momenta up to $q=4$ Å^{-1}; the symbols represent the same modes as in the main plot.

below $q=1.7$ Å^{-1} where a new crossing occurs. Note that the repulsion between these states displayed in Fig. 7 takes place at this momentum too. On the other hand, $F_{\delta_2}(q)$ never approaches the bulk result so much as $F_{\delta_0}(q)$. For momenta larger than q_R all these penetration factors follow curves, which on this scale, are almost parallel to the bulk result. The inset of Fig. 9 will be discussed further below.

Figure 10 shows two pairs of expectation values $V_\kappa^\dagger(q)$ and $V_\kappa(q)$ calculated over a large domain of momenta, $0<q\leqslant 4$ Å^{-1}, compared with $V_L(q)$. These evaluations were carried out for the lowest-lying $\kappa=0$ state and for the δ_0 "resonant mode" and its continuation for $q>q_R$, i.e., the new $\kappa=2$ state. The quantity $V_0^\dagger(q)$ matches $V_0(q)$ shortly below q_R, while $V_{\delta_0}^\dagger(q)$ matches $V_{\delta_0}(q)$ already at the beginning of the maxon region at momentum $q\approx 1.2$ Å^{-1}. In the case of both these branches, once $V_\kappa^\dagger(q)$ and $V_\kappa(q)$ approach one another their values for larger momenta remain indistinguishable in the scale of the figure. An important property of $V_{\delta_0}^\dagger(q)$ and $V_{\delta_0}(q)$ is that when these quantities become almost identical they also approach the very steep particle-hole potential $V_L(q)$. This behavior continues until the repulsion region at $q\approx q_R$, where both couples of expectation values displayed in Fig. 10 approach one another, so that close to the roton minimum we get

$$V_0^\dagger(q)\approx V_0(q)\approx V_{\delta_0}^\dagger(q)\approx V_{\delta_0}(q)\approx V_L(q). \quad (4.11)$$

Following the argumentation of Gernoth *et al.*,[22] since the ripplon excitation of the symmetric film studied in this paper appears to terminate by merging with the bulk excitation curve near the roton minimum (see Fig. 7) leading to

$$\hbar^2\omega_0^2(q\geqslant q_R)=\frac{F_0(q)}{q}\epsilon_0(q)[e_0^\dagger(q)+2V_0^\dagger(q)]\approx\epsilon_0(q)[\epsilon_0(q)+2V_L(q)], \quad (4.12)$$

we may also interpret these lowest-lying modes as rotons trapped in the surface layer. On the other hand, a physically meaningful extension of this kind of analysis can be made. Due to the fact that for momenta corresponding to atomic scale, 1.2 Å$^{-1}\leqslant q\leqslant q_R$, we have $F_{\delta_0}(q)\approx q$, $e_{\delta_0}^\dagger(q)\approx\epsilon_0(q)$ and $V_{\delta_0}^\dagger(q)\approx V_L(q)$, the dispersion curves of the δ_0 "resonant mode" and the bulk excitation are very similar (see Figs. 4 and 7), i.e.,

$$\hbar^2\omega_{\delta_0}^2(q)=\frac{F_{\delta_0}(q)}{q}\epsilon_0(q)[e_{\delta_0}^\dagger(q)+2V_{\delta_0}^\dagger(q)]\approx\epsilon_0(q)[\epsilon_0(q)+2V_L(q)]=\epsilon_L(q). \quad (4.13)$$

Actually, in this momentum regime the trend of both these curves $\hbar^2\omega^2_{\delta_0}(q)$ and $\epsilon_L(q)$ is equal and the energy differences are small, amounting only about 3%. Therefore, for atomic wavelengths, the δ_0 ''resonant mode'' and its bound continuation can be interpreted as a roton trapped at the center of the film, which represents to a good approximation the ''bulk'' excitations of this inhomogeneous system.

In order to complete this part of the study, the particle-hole energies corresponding to the other pairs involved in the repulsions shown in Fig. 7 were also examined. The results for $V_2(q)$, $V^\dagger_{\delta_2}(q)$, and $V^\dagger_{\delta_4}(q)$ are displayed in the inset of Fig. 10. This plot shows that $V^\dagger_{\delta_2}(q)$ and $V^\dagger_{\delta_4}(q)$ are smaller than $V_L(q)$ and $V^\dagger_{\delta_0}(q)$ but, nevertheless, they exhibit very steep slopes similar to that of the bulk particle-hole energy. The latter property gives support to the interpretation of these ''resonant modes'' and their bound continuations as a sort of ''bulk excitation.'' Looking at their wave functions (see, e.g., Figs. 3 and 6) one realizes that the δ_0 mode is an excitation located just at the center of the film and the δ_2 mode is more extended than the previous one, whereas the δ_4 mode is the softest resonance, being spread out over the whole width of the film. On the other hand, the values of $V_2(q)$ indicate a behavior similar to $V_0(q)$ as is expected for a surface mode. Furthermore, the quantity $V_4(q)$, which is not shown in Fig. 10, also exhibits typical characteristics of surface excitations.

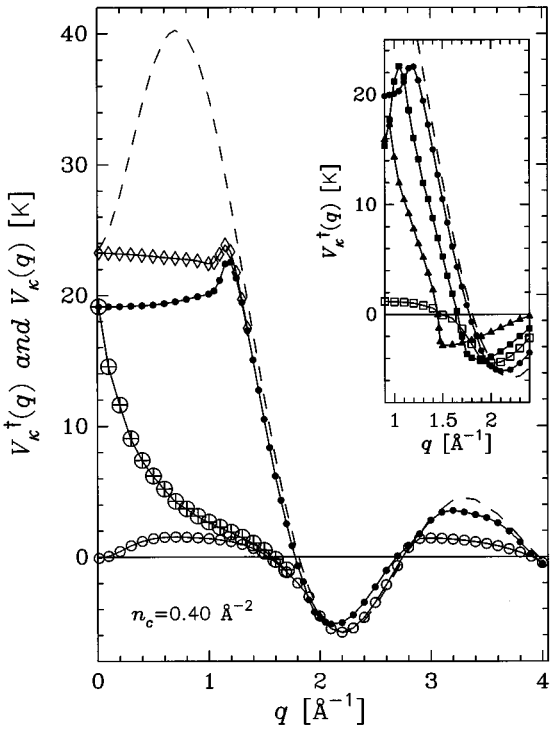

FIG. 10. Particle-hole energies $V^\dagger_\kappa(q)$ and $V_\kappa(q)$ plotted against the wave number q. The symbols ○ and ⊕ stand, in turn, for $V^\dagger_0(q)$ and $V_0(q)$, whereas the symbols ● and ◇ stand for $V^\dagger_{\delta_0}(q)$ and $V_{\delta_0}(q)$, respectively. The dashed curve indicates the particle-hole energy $V_L(q)$ calculated for a bulk liquid at a density of $\rho_L=0.0218$ Å^{-3}. The additional data displayed in the inset, i.e., $V^\dagger_2(q)$, $V^\dagger_{\delta_2}(q)$, and $V^\dagger_{\delta_4}(q)$, are indicated by the symbol □, full solid squares, and solid triangles, respectively.

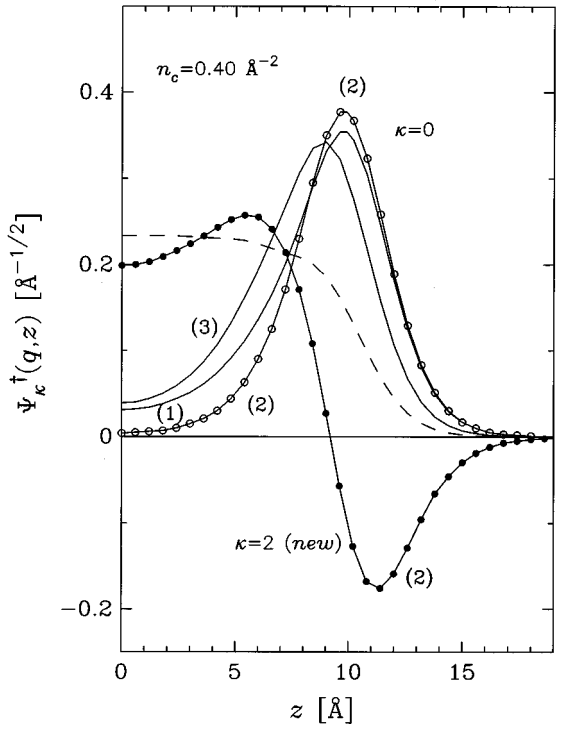

FIG. 11. Wave functions $\psi^\dagger_\kappa(q,z)$ for the two lowest-lying even excitations as a function of z calculated for a few values of momenta of the interval $3.0\leqslant q\leqslant 3.8$ Å^{-1}, where the particle-hole energies $V^\dagger_0(q)$, $V^\dagger_{2\,(\mathrm{new})}(q)$, and $V_L(q)$ displayed in Fig. 10 turn out to be positive for the second time. The dashed curve is the normalized square root of the density profile $\psi_0(q=0,z)=\sqrt{\rho(z)/n_c}$. Curves (1), (2), and (3) correspond, in turn, to $q=3.0$, 3.4, and 3.8 Å^{-1}. All these quantities are symmetric at $z=0$.

Turning to the main plot of Fig. 10, we see that $V_L(q)$ remains negative for $q_R<q\leqslant 2.7$ Å^{-1}. In this region the results for the $\kappa=0$ state coincide with the bulk particle-hole energy, whereas the values of the continuation of $V^\dagger_{\delta_0}(q)$, i.e., the expectation values $V^\dagger_{2\,(\mathrm{new})}(q)$, lie somewhat higher than $V_L(q)$. The typical wave functions of these $\kappa=0$ and 2 (new) states are similar to that plotted in Fig. 6(c).

Figure 10 shows that for larger momenta, $2.8\leqslant q\leqslant 3.9$ Å^{-1}, the particle-hole energies $V^\dagger_0(q)$, $V^\dagger_{2\,(\mathrm{new})}(q)$, and $V_L(q)$ turn out to be positive again, but now both $V^\dagger_0(q)$ and $V^\dagger_{2\,(\mathrm{new})}(q)$ are smaller than $V_L(q)$. By examining the wave functions of the two lowest-lying even states we found that they are surface excitations in this interval. These important novel results are displayed in Fig. 11. It is worthwhile to notice the striking similarity between the curves shown in this plot and the wave functions corresponding to the lowest-lying excitations in a semi-infinite system at low momenta, $0.1\leqslant q\leqslant 0.8$ Å^{-1}, which are displayed in Figs. 4 and 6 of Ref. 22. The latter ones were interpreted physically in terms of surface phonons and capillary waves. In addition, in the case of a symmetric film, the penetration factors for the $\kappa=0$ and 2 (new) states in the $2.8\leqslant q\leqslant 3.9$ Å^{-1} regime are

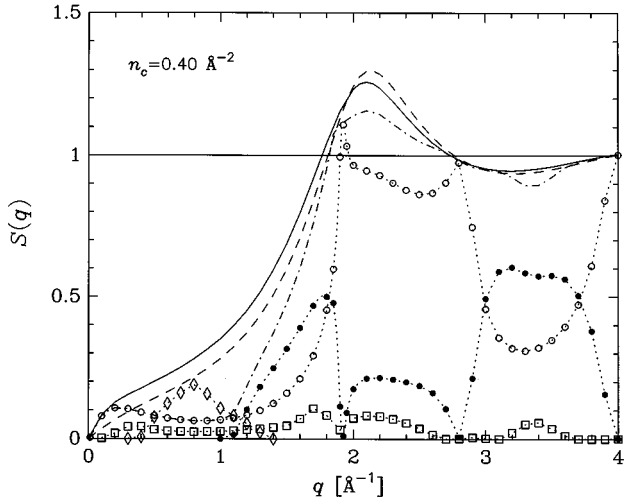

FIG. 12. Static structure function $S(q)$ as a function of momentum. The solid curve is the full static structure function evaluated with (3.17), whereas the dashed line indicates the results calculated for a bulk liquid at a density of $\rho=0.021\,85$ Å^{-3}. The symbols ○, ●, and □ stand, in turn, for the contributions from the lowest-lying $\kappa=0$ mode, the δ_0 "resonant mode," and its bound continuation for $q>q_R$, i.e., the $\kappa=2$ (new) state, and the second branch of even-bound states $\kappa=2$ below the roton minimum and its continuation denoted as the $\kappa=4$ (new) state. The dot-dashed line indicates the sum of the first two of these contributions. The symbol ◇ stands for the contribution originated from the "regular" continuum modes and the δ_6 "resonant mode."

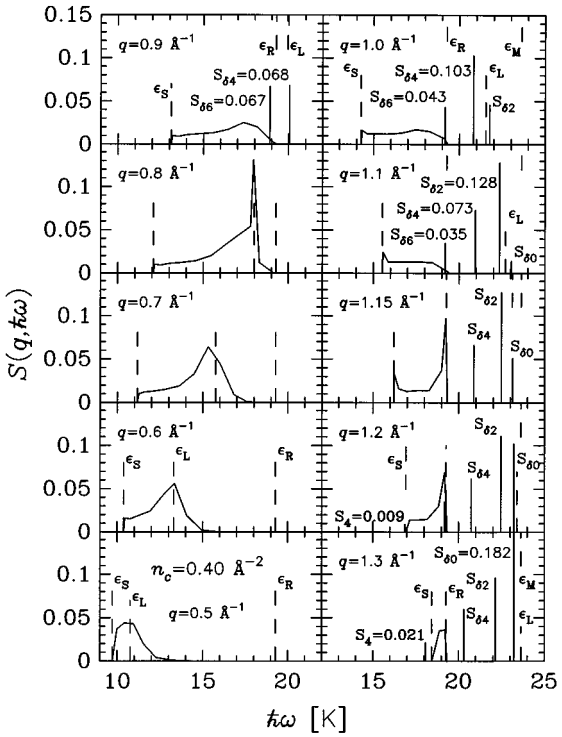

FIG. 13. Diagonal dynamic structure function $S(q,\hbar\omega)$ as a function of energy for several values of momentum. In addition, this plot indicates the strength originated from the δ_0, δ_2, δ_4, and δ_6 "resonant modes" and from the third branch of even-bound states emerging below $\epsilon_S(q)$. In order to have a reference the energies $\epsilon_S(q)$, $\epsilon_L(q)$, ϵ_R, and ϵ_M are also plotted.

almost equal to one another, presenting a departure from the bulk value, as may be seen in the inset of Fig. 9.

D. Liquid structure factors

More information on the structure of the system is revealed by studying the structure functions. Therefore, in this section, we shall examine how the full static structure function in the parallel direction, $S(q)$, is composed of the contributions originating from the different excitations in the film. Along this analysis one must also keep in mind that the character of modes changes with momentum. The solid curve in Fig. 12 shows the full $S(q)$ as a function of momentum obtained by summation of all collective modes according to the expansion (3.17); in addition, for the sake of comparison a dashed curve indicates the results corresponding to a 3D uniform liquid at a density of $\rho_L=0.0218$ Å^{-3}. Figure 12 also shows the size of the partial contributions to the static structure factor given by three special modes: (i) the lowest-lying $\kappa=0$ state, (ii) the δ_0 "resonant mode" and its bound continuation for $q>q_R$, i.e., the $\kappa=2$ (new) state, and (iii) the second branch of even-bound states $\kappa=2$ below the roton minimum and its continuation denoted as the $\kappa=4$ (new) state. Finally, the strength originated from the "regular" continuum part of the spectrum is plotted in this figure too.

Looking at Fig. 12 one realizes that at small momenta, in the region $q<0.2$ Å^{-1}, as a contribution from the $\kappa=0$ mode to $S(q)$ does exhaust the sum rule (3.17). Subsequently, at larger momenta, the ripplon contribution decreases until $q\approx1.0$ Å^{-1} where the trend is reversed. At these intermediate momenta, in the domain $0.40\leqslant q\leqslant1.35$ Å^{-1}, it appears the contribution from the "regular" continuum to the diagonal dynamic structure function $S(q,\hbar\omega)$. This contribution corresponds to excitations lying above the separation energy $\epsilon_S(q)$ and, of course, one must be aware that the "regular" continuum modes obtained from a discretization are really a superposition of many modes in an energy band determined by the box size and the mesh step. Nevertheless, in this case we shall still speak in a broader sense of "modes," but keeping in mind that this denomination is not strictly precise. Figure 13 shows this $S(q,\hbar\omega)$ as a function of energy for several values of q. One can see that for any momentum only excitations of energy lower or approximately equal to ϵ_R provide sizable contributions. For $q<0.9$ Å^{-1} the maximum of strength is centered around $\hbar\omega=\epsilon_L(q)$ and its width decreases for increasing momentum until for $q\approx0.8$ Å^{-1} a well-defined peak is developed. At $q\approx0.9$ Å^{-1} this peak gives rise close to $\hbar\omega=\epsilon_R$ to a "resonant mode" denoted as δ_6, which merges again into the "regular" continuum around $q\approx1.15$ Å^{-1}. The wave function of the δ_6 "resonant mode" evaluated at $q=1.0$ Å^{-1} is displayed in Fig. 14(b). As an illustration of the results for other continuous "modes" in this regime, the wave functions corresponding to those carrying the biggest strength to $S(q,\hbar\omega)$ at $q=0.7$ and 1.3 Å^{-1} are also shown in Figs. 14(a) and 14(c). The δ_6 "resonant mode" lying at $\hbar\omega=19.17$ K is very sharp. In order to corroborate this assertion a neighboring "mode" lying at $\hbar\omega=19.11$ K is also

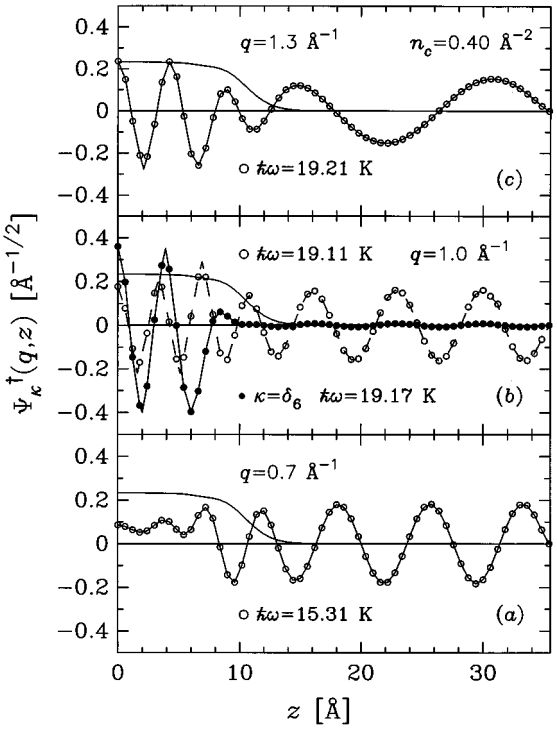

FIG. 14. (a) The continuum mode at $\hbar\omega=15.31$ K carrying the maximum strength for $q=0.7$ Å^{-1} as a function of z. (b) The δ_6 ''resonant mode'' at $\hbar\omega=19.17$ K compared with the ''regular'' continuum mode at $\hbar\omega=19.11$ K, both of them evaluated for $q=1.0$ Å^{-1}. (c) The continuum mode at $\hbar\omega=19.21$ K carrying the maximum strength for $q=1.3$ Å^{-1}. For comparison the solid curve indicates in all the cases the normalized square root of the density profile $\psi_0(q=0,z)=\sqrt{\rho(z)/n_c}$. All these quantities are symmetric at $z=0$.

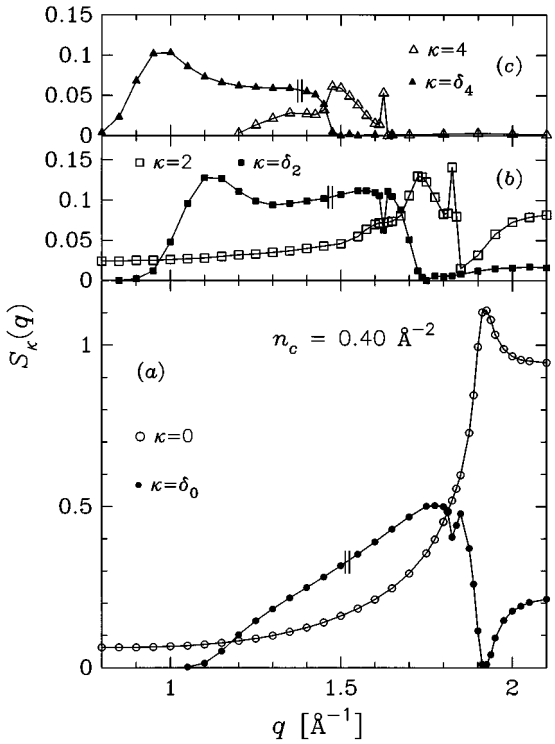

FIG. 15. Partial contributions $S_\kappa(q)$ to the full static structure function originating from bound states and ''resonant modes'' as a function of momentum. The double parallel bars ‖ indicate the place where the ''resonant modes'' become bound states. (a) Contribution from the lowest-lying $\kappa=0$ mode together with that from the δ_0 ''resonant mode'' and its bound continuation. (b) Contribution from the second branch of even-bound states $\kappa=2$ below the roton minimum and its continuation together with the contribution from the δ_2 ''resonant mode'' and its bound continuation. (c) Contribution from the third branch of even-bound states $\kappa=4$ below the roton minimum and its continuation together with the contribution from the δ_4 ''resonant mode'' and its bound continuation.

depicted in Fig. 14(b). In fact, we can see that the latter one, lying only 0.06 K lower than δ_6, already exhibits a typical behavior of a ''regular'' continuum mode. Moreover, it is worthwhile to point out the similarity between the spatial distribution of the δ_6 ''resonant mode'' and the wave functions of the other ''resonant modes'' plotted in Fig. 2 for $q=0.1$ Å^{-1}.

It turns out that the ''regular'' continuum plays a dominant role in the momentum regime $0.5<q<1.1$ Å^{-1}, where it carries the most important contribution to $S(q)$ as is shown in Fig. 12. The data plotted in this figure do also contain the contribution from the δ_6 ''resonant mode,'' the strength of which is indicated in Fig. 13. Of course, its inclusion reinforces considerably the contribution from the continuum to $S(q,\hbar\omega\leqslant\epsilon_R)$ for $0.9\leqslant q\leqslant 1.1$ Å^{-1}. It is interesting to notice that around $q\approx 1.2$ Å^{-1} a bound state emerges from the continuum, giving rise again to the third branch of even-bound states $\kappa=4$ already observed at low momenta; the strength carried by this mode is indicated in Fig. 13. It should be emphasized that for $q>1.5$ Å^{-1} there is no contribution to $S(q)$ from the continuous spectrum at all. The ''regular'' continuum does not contribute anymore and the continuations of the δ_0, δ_2, and δ_4 ''resonant modes'' are already bound states.

Let us now turn back to the $\kappa=0$ mode. Figure 12 shows that for $q>1.0$ Å^{-1} the ripplon contribution to $S(q)$ increases with increasing rate and the δ_0 ''resonant mode'' begins to contribute. The strength of the latter mode grows so rapidly that at $q=1.2$ Å^{-1} it is already bigger than the ripplon one. Both of these contributions become the dominant ones in this regime, amounting to a large part of the total strength as indicated by the dot-dashed curve in Fig. 12. Their simultaneous growth with increasing momentum continues until $q\approx 1.8$ Å^{-1}. This strength enhancement may be followed more cleanly on a finer scale in Fig. 15(a). For momentum $q>1.8$ Å^{-1} the ripplon contribution grows dramatically in such a way that close to the roton minimum it exhausts almost completely the sum rule (3.17) again; of course, on the contrary the contribution from the bound continuation of the δ_0 ''resonant mode'' falls to very small values. The abrupt variation of these contributions, characterized by a strength transfer from the higher-energy state to the lower-energy one, may be attributed to the interaction responsible for the repulsion between the ripplon and the bound continuation of the δ_0 ''resonant mode'' described in a previous section, which also occurs at momenta close to the roton minimum. The almost complete transfer of strength may be related to a some kind of phase transition which is also corroborated by the change of the character of modes depicted in Fig. 6.

Figure 15 also shows partial contributions to the full $S(q)$ stemming from the other two pairs of states undergoing the repulsions displayed in Fig. 7. Although the size of these contributions is much smaller than the magnitude of the dominant ones, data plotted in Figs. 15(b) and 15(c) exhibit a similar transfer of strength to that observed in 15(a). These features occur at the same momenta where the corresponding repulsions take place. Looking at this drawing one realizes that there are a few narrow perturbations of $S_\kappa(q)$. These localized transfers of strength occur at $q=1.725$ and 1.825 Å^{-1}, which correspond to the crossings of the $\kappa=4$ state with the bound continuation of the δ_2 ''resonant mode'' and of the $\kappa=2$ state with the bound continuation of the δ_0 ''resonant mode,'' respectively. In both these cases, when the excitations are approaching one another the state coming from a lower energy captures a piece of strength from the decreasing energy state; subsequently, after the crossing, the captured intensity is given back. Evidence that these are indeed level crossings is provided by the analysis of the wave functions shortly below and shortly above the critical momenta; however, we shall skip the illustration of this argument.

In passing let us point out that there is no change of trend of the strength at any of the double parallel bars indicating in Fig. 15 the momenta at which the ''resonant modes'' become bound states. This is due to the fact that there is no evidence for important changes in the behavior of the corresponding wave functions. The only feature worthy of being mentioned is that the oscillatory components outside of the film still exhibited in Fig. 3 vanish definitively for the new bound states.

In the momentum regime above $q\approx 1.7$ Å^{-1} the contributions of the three modes displayed in Fig. 12 exhaust the sum almost completely, and indeed, as indicated by the dot-dashed curve the largest two contributions already amount to a great part of the full $S(q)$. Finally, it is interesting to note that in the regime where the lowest-lying level clearly becomes a surface state again, i.e., for $3.0\leqslant q\leqslant 3.7$ Å^{-1} (see also Fig. 11), its contribution to $S(q)$ is smaller than that of the first-excited even state. This finding resembles the situation already observed in Fig. 15(a) for $1.2\leqslant q\leqslant 1.8$ Å^{-1}.

E. Interpretation of experimental data of $S(q,\hbar\omega)$

Let us conclude this section comparing theory with experiment. As mentioned in the Introduction, Lauter *et al.*[28] have measured the structure factor $S(q,\hbar\omega)$ of films of atomic thickness. It becomes, therefore, of interest to establish the extent to which the main features of these experimental data can be interpreted on the basis of our results. However, before making this comparison it will be convenient to discuss briefly a shortcoming of the theoretical approach adopted for our calculations and to select an appropriate form of presenting our evaluations.

A well-known result of the calculations carried out for bulk liquid ^{4}He at $T=0$ K within the framework of the original Feynman theory[26] in conjunction with the EL-HNC/0 approximation is that the energies of the phonon-roton spectrum evaluated at the maxon-roton region are too high by a factor of about 2.[3,36] Manousakis and Pandharipande[37] have demonstrated that the agreement with experiment is dramatically improved with the inclusion of the backflow effects introduced by Feynman and Cohen[38] together with three- and four-body distribution functions (the reader may find very interesting comments on the Feynman-Cohen work in the review article of Pines[45]). Quite recently, Clements *et al.*[16] have calculated the excitation spectrum of nonuniform systems by using the CBF approach within a generalized Feynman theory with time-dependent pair correlations treated with the Brilluoin-Wigner perturbation theory (CBF-BW method). Their results are compared in Fig. 9 of Ref. 16 with the experimental data of Ref. 28. From this figure one realizes that theoretical predictions are still too high. Of course, this result is to be expected since from Fig. 2 of Ref. 16 it becomes clear that the CBF-BW approach is not sufficient even to reproduce the experimental data of the 3D uniform liquid. As pointed out by Clements and collaborators, further corrections upon the CBF-BW theory should be included to obtain a better agreement.

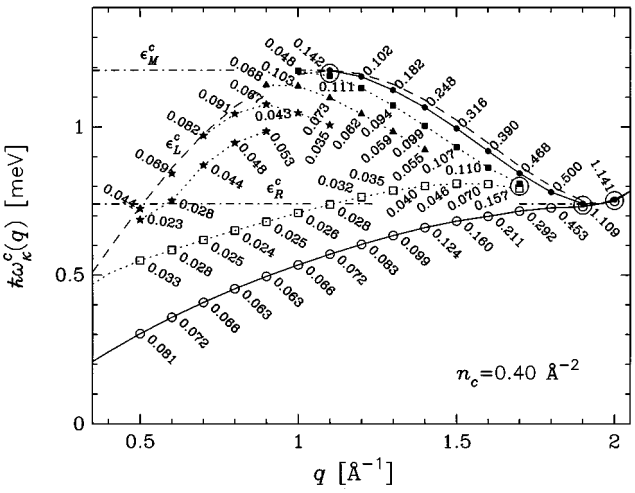

FIG. 16. Corrected excitation spectrum of some even eigenstates as a function of momentum for the film of coverage $n_c=0.4$ Å^{-2}. The open symbols ○ and □ stand for the two lowest-lying bound states, which are surface excitations for $q<q_R$. The excitation energies of the δ_0, δ_2, and δ_4 ''resonant modes'' are indicated, respectively, by solid circles, boxes, and triangles. The stars indicate results for ''regular'' continuum and the δ_6 ''resonant mode.'' Partial contributions $S_\kappa(q)$ to the full static structure function originated from these modes are given. The dashed line is the dispersion relation $\epsilon_L^c(q)$ for a 3D uniform system, while the horizontal dot-dashed lines are the corrected maxon ϵ_M^c and roton ϵ_R^c energies for a bulk liquid at a density of $\rho_L=0.0218$ Å^{-3}.

It is beyond the scope of this paper to carry out any new calculation of corrected dispersion relations since such an evaluation is a task of a great numerical complexity. However, in order to facilitate the comparison of theory with experiment we estimated an improved spectrum, adopting the simplest way to emulate the above-mentioned corrective effects. Namely, we used a scaling procedure in which one assumes that at a fixed value of q the whole calculated excitation spectrum of a nonuniform liquid is depressed by a common factor equal to the ratio $r(q)=\epsilon_L^{\rm expt}(q)/\epsilon_L(q)$ determined from the EL-HNC/0 analysis of the bulk system. In practice, besides the correct phonon-roton bulk spectrum $\epsilon_L^c(q)=r(q)\epsilon_L(q)$ this procedure gives a plausible estima-

tion of all corrected dispersion relations $\hbar\omega_\kappa^c(q) = r(q)\hbar\omega_\kappa(q)$. Figure 16 shows the most important part of the improved inhomogeneous energy spectrum. In this plot, instead of showing a contour map of $S(q,\hbar\omega)$, we directly indicate the strength of the contributions originated from different kind of modes.

Our Fig. 16 for $n_c = 0.4$ Å^{-2} is to be compared with Fig. 1 of Lauter *et al.*[28] where these authors plotted data for a coverage of 0.448 Å^{-2}. It becomes clear that in both these drawings most of the strength is mainly concentrated along two well-defined lines, which correspond to different types of excitations in the system. The excitation energy of the upper curve coincides with the bulk ^{4}He phonon-maxon-roton corrected dispersion relation $\epsilon_L^c(q)$. The contributions lying along this line for $0.5 \leqslant q < 0.9$ Å^{-1} stem from the ''regular'' continuum [note in Fig. 13 that for these momenta the maximum of strength is centered around $\hbar\omega = \epsilon_L(q)$], while in the atomic wavelength regime 0.9 Å$^{-1} \leqslant q < q_R$, they originate from ''resonant modes'' in the first part of the interval and subsequently from the bound continuation of the δ_0 mode. On the other hand, the lowest-lying curve in Fig. 16 is associated with the surface mode analyzed in previous sections. It is interesting to mention that our corrected ripplon energy $\hbar\omega_0^c(q)$ is in good agreement with the dispersion curve calculated by Edwards and Saam[31] with the parameters $a = +1.0$ Å^2 and $\delta = -0.336$ Å, which in turn fits the data of Ref. 28. Moreover, in the caption to Fig. 2 of Ref. 28 the authors point out that for $q = 0.8$ Å^{-1} the bulk phonon lies at $\hbar\omega = 1.05$ meV and the ripplon peak is experimentally found at 0.47 meV, whereas according to our corrected results the corresponding energies are 1.04 and 0.45 meV, respectively. The latter result for the surface excitation, on the one hand, and the satisfactory overall energy pattern exhibited in Fig. 16, on the other, point to a justification *a posteriori* for the use of a common hindrance factor for the whole energy spectrum at each fixed value of momentum. It is expected that the introduced scaling should have no important effect on any other quantity. In passing, we may note that to some extent our results also resemble qualitatively the data displayed in Fig. 13 of Clements *et al.*[16] for $q \leqslant 1.5$ Å^{-1} in the case of coverage $n_c = 0.17$ Å^{-2}.

In order to complete the study it is illuminating to compare along the curves $\epsilon_L^c(q)$ and $\hbar\omega_0^c(q)$ the evolution of the strength obtained from our calculations with the different shades of grey depicted in Fig. 1 of Ref. 28. A feasible way for performing this analysis is to examine the evaluated strength at the momenta where there is a change of gray intensity in that figure. The comparison may begin at $q \simeq 0.5$ Å^{-1} where both branches exhibit an equal shade of gray. Going along the phonon-roton curve towards increasing momenta the first change of gray intensity already occurs at $q \simeq 0.6$ Å^{-1}, where our calculation yields a contribution $S_{p\text{-}r}(q = 0.6) = 0.069$, while the ripplon branch presents the first definitive gray enhancement at $q \simeq 1.1$ Å^{-1} where we obtained $S_0(q = 1.1) = 0.072$. The next change of gray scale along the phonon-roton line takes place at $q \simeq 1.1$ Å^{-1} where the ''resonant modes'' provide a contribution $S_{p\text{-}r}(q = 1.1) = 0.142$ against a value of $S_0(q = 1.5) = 0.160$ obtained close to the corresponding edge on the ripplon curve. Near the subsequent points where the shade becomes darker we get the following pairs of values: $S_{p\text{-}r}(q = 1.5) = 0.316$ to be compared with $S_0(q = 1.7) = 0.292$ and $S_{p\text{-}r}(q = 1.7) = 0.468$ equivalent to $S_0(q = 1.8) = 0.453$. Close to q_R where the total strength is larger than unity the black is reached. All these values show a very good quantitative agreement between the calculated strength and the trend of experimental data. In fact, this is a striking result if one takes into account that for our calculations we assumed that the films are confined by a somewhat unphysical potential.

Furthermore, Fig. 16 also shows that the contributions $S_2(q)$ originating from the second even-bound state are smaller than $S_0(q)$. An analysis of Fig. 1 in Ref. 28 indicates that this fact is quite consistent with the weak shade of gray found experimentally at the corresponding place between the ''bulk'' and ripplon lines for $q \leqslant 1.2$ Å^{-1}. The behavior between these curves for larger momenta is more complex in both discussed figures since in that region there is a larger concentration of contributions.

V. SUMMARY

Properties of the behavior of inhomogeneous systems of liquid ^{4}He at zero absolute temperature have been investigated. Due to the reasons discussed in the Introduction, rather thick films supported by an external potential of the Gaussian form given by (4.1) have been examined. Now, in light of the interesting results obtained in this work, we can state that a study performed by using such a simple potential is well justified. Films of coverages $n_c = 0.3$ and 0.4 Å^{-2} were selected to illustrate the explored features. Here the analysis was focused on the behavior for finite momenta, $q > 0$, since the long-wavelength limit has been already studied in a previous paper.[21] In fact, our results may be considered as complementary to that published by Krotscheck and Tymczak[13] and Clements *et al.*,[15,16] on the one hand, and by Gernoth *et al.*,[22] on the other. The authors of Refs. 13,15,16 investigated the behavior of layered films of various coverages, while Gernoth *et al.*[22] analyzed excitations in the geometry of a half-space.

The present study was performed in two steps: First, we discretized the eigenvalue problems for several different box sizes $z_{\max}$ in order to get excitation energy spectra and the associated wave functions; second, by using the obtained wave function we calculated the matrix elements of the particle-hole potential $V(q,z_1,z_2)$ for the most interesting eigenstates and evaluated the structure function in the parallel direction $S(q,\hbar\omega)$. Let us summarize in the following lines the main findings of this work.

The evolution of the discretized energy spectrum as a function of the box size was explored. Typical results are displayed in Fig. 1. In general, the spectra calculated at a fixed momentum in the regime $0 < q \leqslant 1.5$ Å^{-1} show that the energy of several levels remains constant when $z_{\max}$ is enlarged. These levels correspond to two different sorts of states; in fact, besides the expected bound levels, a few states belonging to the continuum also exhibit such a feature. The latter states also present a special spatial behavior developing large amplitudes inside of the film but having oscillations of smaller amplitudes in the asymptotic regime as displayed in Figs. 2, 3, and 14(b). Therefore, we denoted them as ''resonant modes.'' One must always keep in mind that ''regular''

continuum modes are really a superposition of many modes in an energy band determined by the step of the discretization. However, from the analysis of data like those plotted in Fig. 3 one concludes that the ''resonant'' states have a very narrow width; hence, their energy is defined well enough that one can indeed speak of ''resonant modes.'' Let us mention that in a preliminary report[19] we have already provided some evidence for the existence of this kind of state. Figures 2 and 3 show that these collective excitations present a ''softening'' effect; i.e., the amplitudes outside the film are larger for lower-lying ''resonant modes.''

The wave functions of the discrete states for $q<q_R$ and $\hbar\omega_\kappa(q)<\epsilon_R$ exhibit characteristics of surface excitations. As pointed out in Ref. 22 the number of surface states in the momentum region $0.8\leqslant q\leqslant 1.3$ Å^{-1} depends on the thickness of the system and the strength and width of the external potential. In particular, our results for $n_c=0.3$ and 0.4 Å^{-2}, displayed in Figs. 5 and 4, respectively, seem to confirm the finding of Krotscheck and Tymczak[13] that the number of bound states in this regime decreases with increasing coverage. Furthermore, it is interesting to notice that in the case of the thicker film, $n_c=0.4$ Å^{-2}, two branches of even surface states appear in the spectrum and this is just the same number of branches found by Gernoth *et al.*[22] in the limiting case of a semi-infinite system. The dispersion curves of the ripplon branches shown in Figs. 4 and 5 terminate by merging with the bulk excitation curve near the roton minimum as in the half-space system.

Turning to the ''resonant modes,'' in the regime of large wave numbers corresponding to atomic scale, 1.1 Å$^{-1}<q<q_R$, the analysis of the wave functions $\psi^\dagger_{\delta_n}(q,z)$ (see, e.g., Fig. 3) and the particle-hole matrix elements $V^\dagger_{\delta_n}(q)$ (see Fig. 10) suggests that these $\kappa=\delta_n$ states may be associated with ''bulk'' excitations of the film. In particular, the $\kappa=\delta_0$ mode deserves a special attention; its excitation energy $\hbar\omega_{\delta_0}(q)$ lies very close to the bulk $\epsilon_L(q)$, the matrix element $V^\dagger_{\delta_0}(q)$ almost coincides with $V_L(q)$, and the penetration factor $F_{\delta_0}(q)$ approaches the bulk $F_L(q)=q$. Taking into account these features and the spatial distribution of $\psi^\dagger_{\delta_0}(q,z)$ we interpreted this branch of states in this wave-number range as a roton trapped at the center of the film, where the system is to a good approximation a 3D uniform liquid. The next $\kappa=\delta_2$ mode can be also interpreted in a similar way, even though in this case the wave function $\psi^\dagger_{\delta_2}(q,z)$ is more extended than the former one [cf. Figs. 3(a) and 3(b)] and, in addition, the quantities $\hbar\omega_{\delta_2}(q)$, $V^\dagger_{\delta_2}(q)$ and $F_{\delta_2}(q)$ present larger departures from the bulk results. Finally, the $\kappa=\delta_4$ mode is the softest ''bulk'' excitation being expanded over the whole film. On the other hand, our calculations for films of coverages $n_c=0.22$ (not included in this report), 0.3, and 0.4 Å^{-2} indicate that for increasing n_c the number of ''resonant modes'' increases and the results for $\hbar\omega_{\delta_0}(q)$ and $V^\dagger_{\delta_0}(q)$ approach better the bulk quantities $\epsilon_L(q)$ and $V_L(q)$.

A very interesting phenomenon appears near the roton energy ϵ_R. Figure 7 indicates that the ''resonant modes'' first become bound after crossing with the $\epsilon_S(q)$ curve, and then in the vicinity of ϵ_R all these ''bulk'' excitations undergo repulsions by lower-lying surface excitations. Looking at the energy location of these repulsions it becomes apparent that we can define a stripe around ϵ_R where all these processes take place. Making a connection of this finding with the repulsive effect discussed in Ref. 35, we can state that the behavior of the excitation energies calculated in the present work supports the occurrence of the repulsion between ripplon and bulk levels suggested by Pitaevskii and Stringari on the basis of their calculations performed by assuming a simple mechanism of hybridization.

At the above-mentioned repulsions there is a change of character of the involved modes. The clearest example of this feature is documented in Fig. 6, which shows the evolution of the wave functions of the surface $\kappa=0$ mode and the bound continuation of the $\kappa=\delta_0$ ''resonant mode.'' We should stress that the character of the repelled modes is not exchanged, but there is a real change of it. For instance, Fig. 6 indicates undoubtedly that the surface and bulk modes are transformed into typical zero- and two-node volume wave functions, the geometric shapes of which are completely different from the initial ones.

The size of the partial contributions to the static structure factor $S(q)$ originated from the different kind of modes is displayed in Figs. 12, 13, 15, and 16. Figure 12 shows that at small momenta, $q<0.2$ Å^{-1}, the lowest-lying mode exhausts the sum rule (3.17) and for larger values of q its importance decreases. A further analysis indicates that at intermediate momenta, $0.5\leqslant q\leqslant 1.0$ Å^{-1}, the contributions stemming from ''regular'' continuum modes are the dominant ones. Subsequently, for $1.0<q<1.7$ Å^{-1} the ''resonant modes'' and their bound continuations carry the largest contributions to $S(q)$ (see Fig. 15). An interesting phenomenon occurs close to the momenta corresponding to the repulsions displayed in Fig. 7. As shown in Fig. 15, in the vicinity of such momenta there is an almost total transfer of strength from the ''bulk'' excitations to the lower-lying surface ones. In particular, at $q\approx q_R$ there is a dramatic, due to the large size of involved strengths, transfer from the bound continuation of the $\kappa=\delta_0$ ''resonant mode'' to the $\kappa=0$ surface mode. The latter behavior may be interpreted as further evidence for a sort of phase transition of the system; remember that this conclusion is also supported by the change of character of both these modes found just around q_R. Finally, we should point out that for $q>q_R$ the sum of the contributions originating from the two lowest-lying even states reproduces the main features of the behavior of $S(q)$, and if one also adds the strength carried by the second-excited even state, the sum rule (3.17) becomes, in practice, exhausted (see Figs. 12 and 15).

On the basis of the results reported in the present paper, one can understand the main features exhibited by the contour plot of the measured inelastic structure factor $S(q,\hbar\omega)$ shown in Fig. 1 of Ref. 28. The experimental fact that the strength is mainly concentrated along the bulk $\epsilon^c_L(q)$ and ripplon $\hbar\omega^c_0(q)$ excitation curves is reproduced by our calculation. In addition, our approach is also able to account for the quantitative evolution of the strength as a function of the wave number q. Perhaps, it is worthy of notice that multiplying the whole spectrum by a hindrance factor derived from the analysis of bulk fluid, which therefore only depends on the momentum, one obtains a satisfactory corrected spec-

trum and, in particular, a good approximation for the ripplon excitation energy. The striking similarity between our Fig. 16 for $n_c=0.4$ Å^{-2} and Fig. 1 of Ref. 28 for $n_c=0.448$ Å^{-2} suggests that for films of large coverages the main features of the contour map of $S(q,\hbar\omega)$ for $q\geqslant 0.5$ Å^{-1} might not be very sensitive to details of the external substrate potential.

Another new result of this work is the finding of a second region where the ground-state excitations are surface modes. This feature occurs for $2.9\leqslant q\leqslant 3.9$ Å^{-1} where the particle-hole energies $V_0^{\dagger}(q)$ and $V_{2\,(\mathrm{new})}^{\dagger}(q)$ are positive again. The corresponding wave functions are displayed in Fig. 11. The change of the geometric shape of these modes is also manifested in other quantities like $F_0(q)$ and $F_{2\,(\mathrm{new})}(q)$ (see inset of Fig. 9) as well as $S_0(q)$ and $S_{2\,(\mathrm{new})}(q)$ (look at Fig. 12).

All told, we may have a reasonable confidence in our theoretical calculation, giving a strong support to the CBF method for treating boson quantum fluids. Moreover, one could conjecture that the simplest EL-HNC/0 approximation for the ground state together with the original Feynman approach for elementary excitations already contains the essential physical information needed for a plausible qualitative description of the behavior of the system. In this context, any more elaborated theoretical approach would mainly provide a better quantitative agreement, so that the inclusion of higher-order correlations[3,36,37] and backflow effects as those introduced by Feynman and Cohen[38] would primarily improve the quantitative description of an inhomogeneous system as happens in the case of the a uniform fluid. However, to get accurate results it is, of course, of great importance too. Therefore it is worthwhile to point out that, since the CBF theory affords a systematic way of incorporating backflow correlations,[3,4] it is expected that a future inclusion of such effects will not pose any formal difficulties.

ACKNOWLEDGMENTS

This work was supported, in part, by the Fundación Antorchas of Argentina. The author thanks Professor F. Bary Malik for stimulating discussions at the early stage of this work.

APPENDIX: POTENTIALS FOR THE OPTIMIZATION EQUATIONS

The generalized Hartree potential needed for the determination of the optimal local density $\rho(z)$ is

$$V_H(z_1)=\int_{-\infty}^{\infty} dz_2\rho(z_2)W_H(z_1,z_2). \tag{A1}$$

For the calculations carried out in the present work we adopted for $W_H(z_1,z_2)$ the formula derived by Saarela *et al.*,[5]

$$W_H(z_1,z_2)=2\pi\int_0^{\infty}\eta d\eta\Big(g(\eta,z_1,z_2)v(r_{12})+\frac{\hbar^2}{2m}[|\nabla_1\sqrt{g(\eta,z_1,z_2)}|^2+|\nabla_2\sqrt{g(\eta,z_1,z_2)}|^2]$$
$$-\frac{\hbar^2}{8m}[\nabla_1 g(\eta,z_1,z_2)\cdot\nabla_1 N(\eta,z_1,z_2)+\nabla_2 g(\eta,z_1,z_2)\cdot\nabla_2 N(\eta,z_1,z_2)]-\frac{\hbar^2}{8m}\nabla_2 N(\eta,z_1,z_2)\cdot\nabla_2 X(\eta,z_1,z_2)\Big), \tag{A2}$$

with

$$r_{12}=\sqrt{\eta^2+(z_2-z_1)^2}. \tag{A3}$$

The "particle-hole" (p-h) interaction $V_{p\text{-}h}(q,z_1,z_2)$ required in the PPA procedure is the Hankel transform (2.9) of the potential defined by (3.17) of Ref. 6:

$$V_{p\text{-}h}(\eta,z_1,z_2)=g(\eta,z_1,z_2)v(r_{12})+\frac{\hbar^2}{2m}[|\nabla_1\sqrt{g(\eta,z_1,z_2)}|^2+|\nabla_2\sqrt{g(\eta,z_1,z_2)}|^2]$$
$$+[g(\eta,z_1,z_2)-1]\left[\frac{\hbar^2}{4m}[D(1)+D(2)]N(\eta,z_1,z_2)+V_C(\eta,z_1,z_2)\right]. \tag{A4}$$

Here $D(i)$ is the abbreviated derivative,

$$D(i)=\nabla_{\eta}^2+\frac{1}{\rho(z_i)}\frac{d}{dz_i}\rho(z_i)\frac{d}{dz_i}, \tag{A5}$$

where ∇_η^2 is the Laplace operator in the x-y plane. The quantity $V_C(\eta,z_1,z_2)$ is a convolution-type contribution which can be conveniently expressed in momentum space as

$$V_C(q,z_1,z_2)=-\frac{1}{2}\int_{-\infty}^{\infty}dz_3X(q,z_1,z_3)H(q,z_3)X(q,z_3,z_2). \tag{A6}$$

*Also at the Carrera del Investigador Científico of the Consejo Nacional de Investigaciones Científicas y Técnicas, Av. Rivadavia 1917, RA–1033 Buenos Aires, Argentina.

[1] E. Cheng, M.W. Cole, J. Dupont-Roc, W.F. Saam, and J. Treiner, Rev. Mod. Phys. **65**, 557 (1993).

[2] J.W. Clark and E. Feenberg, Phys. Rev. **113**, 388 (1959).

[3] E. Feenberg, *Theory of Quantum Fluids* (Academic, New York, 1969).

[4] J.W. Clark, in *Progress in Particle and Nuclear Physics*, edited by D. Wilkinson (Pergamon, New York, 1979), Vol. 2, p. 89.

[5] M. Saarela, P. Pietiläinen, and A. Kallio, Phys. Rev. B **27**, 231 (1983).

[6] E. Krotscheck, G.-X. Qian, and W. Kohn, Phys. Rev. B **31**, 4245 (1985).

[7] E. Krotscheck, Phys. Rev. B **31**, 4258 (1985).

[8] E. Krotscheck, Phys. Rev. B **32**, 5713 (1985).

[9] E. Krotscheck, S. Stringari, and J. Treiner, Phys. Rev. B **35**, 4754 (1987).

[10] J.L. Epstein and E. Krotscheck, Phys. Rev. B **37**, 1666 (1988).

[11] S.A. Chin and E. Krotscheck, Phys. Rev. Lett. **65**, 2658 (1990).

[12] E. Krotscheck and C.J. Tymczak, in *Excitations in Two-Dimensional and Three-Dimensional Quantum Fluids*, Vol. 257 of NATO Advanced Study Institute, Series B: Physics, edited by A.F.G. Wyatt and H.J. Lauter (Plenum, New York, 1991), p. 257.

[13] E. Krotscheck and C.J. Tymczak, Phys. Rev. B **45**, 217 (1992).

[14] B.E. Clements, E. Krotscheck, and H.J. Lauter, Phys. Rev. Lett. **70**, 1287 (1993).

[15] B.E. Clements, J.L. Epstein, E. Krotscheck, and M. Saarela, Phys. Rev. B **48**, 7450 (1993).

[16] B.E. Clements, H. Forbert, E. Krotscheck, H.J. Lauter, M. Saarela, and C.J. Tymczak, Phys. Rev. B **50**, 6958 (1994).

[17] L. Szybisz and M.L. Ristig, Phys. Rev. B **40**, 4391 (1989).

[18] L. Szybisz, Phys. Rev. B **41**, 11 282 (1990).

[19] L. Szybisz and R.O. Vallejos, in *Proceedings of the XV International Workshop on Condensed Matter Theories*, Mar del Plata, Argentina, 1991, edited by A. N. Proto and J. L. Aliaga (Plenum, New York, 1992), Vol. 7, p. 107.

[20] L. Szybisz, Z. Phys. B **90**, 341 (1993).

[21] L. Szybisz, Z. Phys. B **96**, 235 (1994).

[22] K.A. Gernoth, J.W. Clark, G. Senger, and M.L. Ristig, Phys. Rev. B **49**, 15 836 (1994).

[23] K.A. Gernoth, Ph.D. thesis, Universität zu Köln, Germany, 1990.

[24] K.A. Gernoth and M.L. Ristig, Phys. Rev. B **45**, 2969 (1992).

[25] K.A. Gernoth, J.W. Clark, G. Senger, and M.L. Ristig, in *Proceedings of the XVI International Workshop on Condensed Matter Theories*, San Juan, Puerto Rico, 1992, edited by L. Blum and F.B. Malik (Plenum, New York, 1993), Vol. 8, p. 195.

[26] R.P. Feynman, Phys. Rev. **94**, 262 (1954).

[27] E. Cheng, W.F. Saam, M.W. Cole, and J. Treiner, J. Low Temp. Phys. **92**, 11 (1993).

[28] H.J. Lauter, H. Godfrin, V.L.P. Frank, and P. Leiderer, Phys. Rev. Lett. **68**, 2484 (1992).

[29] H.J. Lauter, H. Godfrin, and P. Leiderer, J. Low Temp. Phys. **87**, 425 (1992).

[30] C.C. Chang and M. Cohen, Phys. Rev. B **11**, 1059 (1975).

[31] D.O. Edwards and W.F. Saam, in *Progress in Low Temperature Physics*, edited by D.F. Brewer (North-Holland, Amsterdam, 1978), Vol. 7A, p. 282.

[32] G. Ji and M. Wortis, Phys. Rev. B **34**, 7704 (1986).

[33] K.R. Atkins, Can. J. Phys. **31**, 1165 (1953); Phys. Rev. **113**, 962 (1959).

[34] D.O. Edwards, J.R. Eckardt, and F.M. Gasparini, Phys. Rev. A **9**, 2070 (1974).

[35] L. Pitaevskii and S. Stringari, Phys. Rev. B **45**, 13 133 (1992).

[36] C.E. Campbell and F.J. Pinski, Nucl. Phys. **A328**, 210 (1979).

[37] E. Manousakis and V.R. Pandharipande, Phys. Rev. B **30**, 5062 (1984).

[38] R.P. Feynman and M. Cohen, Phys. Rev. **102**, 1189 (1956).

[39] L.S. Ornstein and F. Zernike, Proc. Acad. Sci. Amsterdam **17**, 793 (1914).

[40] T. Morita and K. Hiroike, Prog. Theor. Phys. **25**, 537 (1961).

[41] C.E. Campbell, in *Progress in Liquid Physics*, edited by C.A. Croxton (Wiley, New York, 1978), Chap. 6, p 213.

[42] W.L. McMillan, Phys. Rev. **138**, A442 (1965).

[43] D. Schiff and L. Verlet, Phys. Rev. **160**, 208 (1967).

[44] R.A. Aziz, V.P.S. Nain, J.S. Carley, W.L. Taylor, and G.T. McConville, J. Chem. Phys. **70**, 4330 (1979).

[45] D. Pines, Phys. Today **42**(2), 61 (1989).